Quasi-Lagrangian Large Eddy Simulations of Cross-Equatorial Flow in the East Pacific Atmospheric Boundary Layer

S. P. DE SZOEKE AND C. S. BRETHERTON

Department of Atmospheric Sciences, University of Washington, Seattle, Washington

(Manuscript received 8 August 2003, in final form 17 December 2003)

ABSTRACT

Using a large eddy simulation (LES), the atmospheric boundary layer (ABL) is numerically modeled along 95°W from 8°S to 4°N during boreal autumn, and compared to observations from the East Pacific Investigation of Climate Processes in the Coupled Ocean–Atmosphere System (EPIC) 2001. Since the local ABL winds are predominantly southerly in this season, a ''quasi-Lagrangian'' forcing is used in which the ABL air column is forced as if it were advecting northward with the mean September–October 2001 meridional wind across the equatorial cold tongue and the rapidly warming SSTs to the north. Pressure gradients and large-scale zonal advective tendencies are prescribed as a function of latitude. Where possible, observations from the EPIC 2001 experiment are used for forcing and for comparison with model results.

The ABL's modeled vertical structure accords with the conceptual model of Wallace et al. and agrees well with observations. Surface stability accounts for the minimum in surface wind over the equatorial cold tongue and the maximum over the warm water to the north. Stability of the lower ABL over the cold tongue allows a jet to accelerate at about 500-m height, relatively uncoupled to the frictional surface layer. Vertical mixing over the warm water to the north distributes this momentum to the surface.

Additional simulations were performed to explore the modeled ABL's sensitivity to pressure gradients, zonal advection, free-tropospheric humidity, and initial conditions. The model ABL was robust: changing the forcings resulted in little change in the modeled structure. The strongest sensitivity was of stratocumulus clouds over the cold tongue to cloud-top radiative cooling. Once formed at the southern edge of the cold tongue, modeled stratocumulus clouds demonstrate a remarkable ability to maintain themselves over the cold tongue in the absence of surface fluxes by radiative cooling at their tops. The persistence of thin stratocumulus clouds in this Lagrangian model suggests that horizontal advection of condensate might be an important process in determining cloudiness over the cold tongue.

1. Introduction

Processes that affect surface winds in the Tropics are advection of momentum, surface pressure gradients (Deser 1993), momentum fluxes through the top of the ABL (e.g., Stevens et al. 2002), and efficiency of turbulent vertical mixing within the ABL. Lindzen and Nigam (1987) noted that above warm SST, lower-tropospheric air temperature is warm, hydrostatically inducing low surface pressure. The corresponding horizontal pressure gradients induce horizontal wind convergence over warm SST, explaining the large-scale distribution of precipitation over the Tropics. According to the Lindzen–Nigam theory, winds near the equator should be particularly strong over large SST gradients, such as the winds seen over the eastern equatorial Pacific during boreal fall.

Wallace et al. (1989, hereafter WMD) suggested that in this region, vertical mixing within the ABL also modulates the coupling of surface wind to SST. Especially in July–December, a large-scale meridional pressure gradient in the east Pacific causes cross-equatorial ABL flow, while oceanic upwelling creates a tongue of cold water along the equator. WMD found that surface winds reported in a climatology of routine ship observations were strongest over the warm water to the north of the strongest SST gradients. They proposed that the surface wind is stronger where the SST is significantly warmer than the surface air temperature (an unstable surface layer), because turbulent convection efficiently mixes momentum down to the surface. Conversely, over cold SST, the surface layer is more stable and inhibits downward turbulent mixing of momentum, weakening the surface wind. The signature of the stability effect on the surface wind is horizontal divergence across (positive downwind) SST gradients.

Hayes et al. (1989) and Thum et al. (2002), using Tropical Atmosphere Ocean (TAO) buoy observations, and Chelton et al. (2001), using satellite observations, showed how surface wind variations in this region correlated with meandering of the pronounced equatorial

Corresponding author address: S. P. de Szoeke, Dept. of Atmospheric Sciences, University of Washington, Seattle, WA 98195.
E-mail: deszoeke@atmos.washington.edu

© 2004 American Meteorological Society

front in SST associated with tropical instability waves. These correlations were consistent with the mechanism of WMD. Also consistent with the WMD mechanism, Bond (1992) used radiosonde observations taken during TAO buoy maintenance cruises to show a lower surface wind speed and an elevated wind jet in the ABL over the cold tongue, and increased surface wind speed with vertically homogeneous winds within the ABL over the warm water north of the SST front. Hashizume et al. (2002) found similar results from a research cruise that cut zonally through several meanders of the SST front.

During September–October 2001, the East Pacific Investigation of Climate Processes in the Coupled Ocean–Atmosphere System (EPIC) 2001 field campaign made intensive measurements of the atmospheric and oceanic structure along the easternmost line of TAO buoys at 95°W (Raymond et al. 2004). One goal of these measurements was to provide a comprehensive view of the mean ABL structure and its day-to-day variability in the cross-equatorial flow region. By combining airborne, ship-based, and TAO buoy measurements, EPIC 2001 for the first time documented the ABL turbulence, cloud structures and microphysics, radiative flux profiles, and instantaneous downwind evolution over a representative range of atmospheric conditions. This provides an excellent opportunity to extend WMD's ideas into a rigorous, quantitative test of ABL models and general circulation model (GCM) parameterizations in this challenging and climatically important region.

In this paper, we adopt the large eddy simulation (LES) as a natural modeling approach for better understanding the eastern equatorial Pacific ABL, and for interpreting and comparing with the EPIC 2001 observations. Because the largest turbulent structures are resolved, the LES framework is capable of simulating the interactions of surface fluxes, turbulence, clouds, and radiation that contribute to the vertical structure of the ABL and its south-to-north evolution. Using a ''quasi-Lagrangian'' LES approach described in section 2, we simulate ABL evolution along 95°W, starting at 8°S in the southeast Pacific stratocumulus region (Bretherton et al. 2004), traversing the cold tongue and the equatorial SST front, and ending at 4°N in the shallow cumulus region upstream of the intertropical convergence zone. We compare our simulations with EPIC 2001 observations (section 3), and present sensitivity studies (section 4), followed by discussion and conclusions (section 5). The LES is consistent with WMD, but it elucidates several other feedbacks that may affect the vertical structure and temporal variability of the ABL cross-equatorial flow. Our quasi-Lagrangian LES models the thermodynamic evolution and vertical structure of the ABL well, but pressure gradients are prescribed and do not respond to the evolving ABL.

2. Methods

We integrated an LES on a 3-km cubic domain with enough resolution to resolve turbulent eddies 100 m or more across. The LES was forced in a quasi-Lagrangian manner, by time-varying conditions (notably underlying SST, large-scale pressure gradients, and overlying free-tropospheric temperature and humidity) that correspond to the northward movement undergone by a typical boundary layer air column. The simulation can then be understood as tracing the boundary layer column's evolution with time or latitude as the column moves along 95°W. Section 2a describes the quasi-Lagrangian framework and how the external forcings are applied to the LES. Section 2b describes how observations and reanalysis are used to determine these latitude-dependent external forcings. Section 2c describes the details of the LES model.

a. Quasi-Lagrangian method

Our quasi-Lagrangian forcing strategy was inspired by Wakefield and Schubert (1981), Wyant et al. (1997), and Bretherton et al. (1999a). A meridional ABL trajectory (latitude versus time) was computed from the September–October 2001 National Centers for Environmental Predicition (NCEP) mean 1000–925-hPa wind, which we assume to represent the mean meridional ABL wind. Along this trajectory, it takes 3 days to get from 8°S to 4°N. Our strategy capitalizes on the predominantly southerly winds near the equator and the weak zonal gradient of SST compared to the meridional gradient. This ensures that advective tendencies are primarily due to the meridional wind. To simplify the model and facilitate comparison with EPIC 2001 observations—which were all along a single longitude—we neglected the zonal velocity from the Lagrangian advective wind speed. The idealized Lagrangian trajectory is a straight northward path along 95°W longitude. Large-scale meridional advection is built into this Lagrangian column-following formulation, while large-scale zonal advection is computed from the NCEP reanalysis and then applied to the LES in an Eulerian fashion.

In the quasi-Lagrangian formulation, the entire column is assumed to move at the mean ABL meridional velocity. A shortcoming of this method is that it does not simulate the effect of differential meridional advection at different heights within the ABL. If there is vertical shear in the boundary layer, then air moving faster or slower than the vertical mean could contribute an advective tendency into the ABL column. In the LES, even though the layers are free to move at different speeds, the small domain and periodic lateral boundaries prevent differential advection into the column. This shortcoming is of minimal importance as long as the boundary layer is mixed, because in this case the velocities do not change with height. To the extent that the ABL is not well mixed, differential advection would have an effect not simulated by the quasi-Lagrangian method. While the ABL evolution is predicted in our simulation, the free troposphere is merely specified as an upper boundary condition for the ABL by relaxing

it to a specified profile on an hourly time scale. Externally relaxing the free troposphere provides for the effect of differential meridional advection between the ABL and the free troposphere.

The evolution of the vertical structure of the boundary layer is predicted by the LES as if it were a turbulence-resolving column model, with horizontally homogeneous large-scale forcings. We use the Ogura and Phillips (1962) anelastic equations to describe motions within the column. These are based on hydrostatic profiles of reference pressure $p_0(z)$ and density $\rho_0(z)$ calculated assuming a constant reference potential temperature θ_{00} = 302.1 K and a reference surface pressure $p_0(0)$ = 1012.8 hPa:

$$\frac{D\mathbf{u}}{Dt} = g\frac{\theta_v'}{\theta_{00}}\mathbf{k} - \boldsymbol{\nabla}\phi' - f\mathbf{k}\times\mathbf{u} + \mathbf{S}^{\mathbf{u}}_{\mathrm{LS}} + \mathbf{S}^{\mathbf{u}}_{\mathrm{sfc}} + \frac{1}{\rho_0}\boldsymbol{\nabla}\cdot\rho_0 K_M\boldsymbol{\nabla}\mathbf{u}, \quad (1)$$

$$\frac{D\theta_l}{Dt} = S^{\theta_l}_{\mathrm{micro}} - \frac{1}{\rho_0 C_P \Pi_0}\frac{\partial}{\partial z}F_{\mathrm{rad}} + S^{\theta_l}_{\mathrm{LS}} + S^{\theta_l}_{\mathrm{sfc}} + \frac{1}{\rho_0}\boldsymbol{\nabla}\cdot\rho_0 K_H\boldsymbol{\nabla}\theta_l, \quad (2)$$

$$\frac{Dq_t}{Dt} = S^{q_t}_{\mathrm{micro}} + S^{q_t}_{\mathrm{LS}} + S^{q_t}_{\mathrm{sfc}} + \frac{1}{\rho_0}\boldsymbol{\nabla}\cdot\rho_0 K_H\boldsymbol{\nabla}q_t, \quad (3)$$

$$\frac{Dq_r}{Dt} = -S^{q_t}_{\mathrm{micro}} - w_r\frac{\partial q_r}{\partial z}, \quad (4)$$

$$\boldsymbol{\nabla}\cdot(\rho_0\mathbf{u}) = 0. \quad (5)$$

The left-hand side of Eqs. (1)–(4) are the Lagrangian time derivatives of velocity $\mathbf{u}$, liquid water potential temperature θ_l, water mixing ratio q_t (including vapor and cloud liquid), and rain water mixing ratio q_r. Primes indicate the deviation of a quantity from its horizontal mean. The Coriolis force $-f\mathbf{k}\times\mathbf{u}$ is computed explicitly by the LES. The heat source due to evaporation and condensation of cloud water does not appear because the equations have been formulated in terms of liquid water potential temperature,

$$\theta_l = \theta - (L/\Pi_0 C_p)q_l, \quad (6)$$

where θ is the potential temperature, L is the latent heat of vaporization of water, Π_0 is the base-state Exner function, C_p is the specific heat of air, and q_l is the cloud liquid water. There is, however, a θ_l source $S^{\theta_l}_{\mathrm{micro}}$, and a corresponding q_t sink $S^{q_t}_{\mathrm{micro}}$ when precipitation forms from cloud liquid water, or evaporates (detailed in section 2c). The source S_{sfc} due to the surface flux is deposited entirely in the lowest model level. The radiative flux convergence $-\partial F_{\mathrm{rad}}/\partial z$ is calculated columnwise by a radiative transfer model within the LES. The last terms in Eqs. (1)–(3) are the subgrid-scale diffusion of momentum, heat, and moisture. The subgrid eddy viscosity is denoted K_M and K_H is the eddy diffusivity of heat and moisture. Anelastic mass continuity is expressed by (5).

We denote specified latitude and height-dependent quantities derived from EPIC 2001 or NCEP by a hat, and denote horizontally domain-averaged quantities predicted by the LES by an overbar. Then the large-scale forcings are given by

$$S^{\mathbf{u}}_{\mathrm{LS}} = H(z - z_{\mathrm{relax}})\frac{(\hat{\mathbf{u}} - \overline{\mathbf{u}})}{\tau} - \hat{u}\frac{\partial\hat{\mathbf{u}}}{\partial x} - \hat{w}\frac{\partial\overline{\mathbf{u}}}{\partial z} - \boldsymbol{\nabla}\hat{\phi}, \quad (7)$$

$$S^{\theta_l}_{\mathrm{LS}} = H(z - z_{\mathrm{relax}})\frac{(\hat{\theta}_l - \overline{\theta_l})}{\tau} - \hat{u}\frac{\partial\hat{\theta}_l}{\partial x} - \hat{w}\frac{\partial\overline{\theta_l}}{\partial z}, \quad \text{and} \quad (8)$$

$$S^{q_t}_{\mathrm{LS}} = H(z - z_{\mathrm{relax}})\frac{(\hat{q}_t - \overline{q_t})}{\tau} - \hat{u}\frac{\partial\hat{q}_t}{\partial x} - \hat{w}\frac{\partial\overline{q_t}}{\partial z}. \quad (9)$$

The first terms in the large-scale forcing Eqs. (7)–(9) are the relaxation of the mean to the prescribed sounding above the ABL. The Heaviside function $H(z - z_{\mathrm{relax}})$ is unity above the relaxation height z_{relax} and zero below. The relaxation height

$$z_{\mathrm{relax}} = \overline{z_{\mathrm{inv}}} + 150\ \mathrm{m} \quad (10)$$

is defined as 150 m above the horizontal mean inversion height. In each column the inversion height z_{inv} is defined to be the height of maximum stability $\partial\theta_v/\partial z$. A short relaxation time scale, arbitrarily chosen as τ = 1 h, keeps the free troposphere close to the specified thermodynamic and wind profiles above the relaxation height. The relaxation height was chosen to be as close as possible to the inversion while still remaining above the maximum height of inversion-penetrating turbulent eddies. This ensures the free-tropospheric air entrained into the boundary layer has the desired specified thermodynamic characteristics, but does not distort the inversion structure. A similar procedure was used by Wyant et al. (1997).

The large-scale zonal advection $-\hat{u}\partial(\hat{})/\partial x$ and pressure gradient term $-\boldsymbol{\nabla}\hat{\phi}$ are computed from NCEP reanalysis. The vertical advection $-\hat{w}\partial(\overline{\ })/\partial z$ is due to the imposed subsidence velocity $\hat{w}$. The mean subsidence is incorporated in the LES by applying vertical advective tendencies to the prognosed quantities of $\overline{\theta}_l$, $\overline{q}_t$, $\overline{u}$, and $\overline{v}$, without changing the LES-predicted vertical velocity (which always has zero horizontal mean). The large-scale meridional advection is accounted for by the quasi-Lagrangian boundary conditions on the LES.

b. Large-scale forcing

The required time-dependent forcings on the LES are 1) sea surface temperature; 2) zonal advection; 3) pressure gradient force; 4) subsidence rate; and 5) free-tropospheric profiles of temperature, humidity, and wind. We composited the SST from the Tropical Rainfall Measuring Mission (TRMM) Microwave Imager (TMI) average satellite retrievals for 30 September–2 October 2001, and 5-cm-deep temperatures measured from the

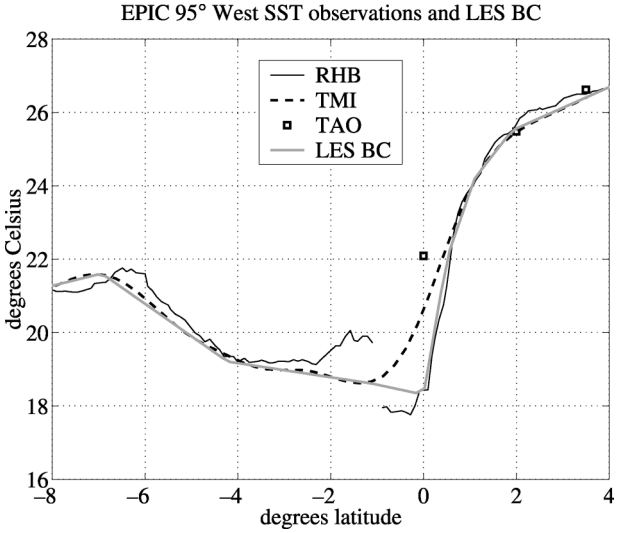

FIG. 1. SST along 95°W measured by two partial *RHB* transects, 30 Sep–2 Oct 2001 average TMI observations, and Sep–Oct 2001 mean TAO buoy observations. The line labeled LES BC is the boundary condition used for the LES.

National Oceanic and Atmospheric Administration's (NOAA) R/V *Ronald H. Brown* (*RHB*; see Fig. 1). The TMI SST is smooth compared to the *RHB* SST, which was sampled during a single southward transect (thereby convolving spatial and temporal variability). The thin gray line in Fig. 1 shows the composite SST that we used for LES integration. It mostly follows the TMI retrieval, but near 0.5°N, we have chosen to sharpen the idealized SST front in agreement with the observations from the *RHB* (thin lines). We do this because we regard our simulation as one typical realization of ABL evolution over a sharp SST front, not as a 2-month composite averaging over all the day-to-day oceanic and atmospheric variability.

Zonal advection and large-scale pressure gradient forces are computed from the September–October 2001 mean NCEP reanalysis. They are computed at the levels available in the NCEP reanalysis dataset: the surface, 1000, 925, 850, and 700 hPa. The sea level pressure gradient force $-\rho_0^{-1}\nabla p(0)$ is used at the surface, while the geopotential height gradient $-\nabla\phi$ is used at the reanalysis pressure levels. The geopotential gradients are assigned a nominal altitude and interpolated in z to the model grid levels. The large-scale zonal pressure gradient force $-\partial\hat{\phi}/\partial x$ is computed with a centered difference of geopotential between 92.5° and 97.5°W. The large-scale meridional pressure gradient force $-\partial\hat{\phi}/\partial y$ is computed from the difference of the geopotential at 2.5° latitude intervals (. . . , −2.5°, 0°, 2.5°, . . .) along 95°W. The meridional geopotential gradients are centered in between (. . . , −1.25°, 1.25°, . . .) and then linearly interpolated in y to all latitudes to provide a continuous forcing. This procedure yields a cross section of large-scale forcings that depend on latitude y and altitude z.

Figure 2 shows these forcing terms. The effect of zonal temperature and moisture advection (Figs. 2a,b) is to cool and dry the near surface air. In the south, there is a considerable zonal component to the SST gradient. The easterly wind component advects air that has been in contact with the cool upwelled water along the South American coast. Over the cold tongue, where the air–sea temperature difference is positive, the advective cooling and drying is small but significant, because other thermal forcings are small.

The zonal pressure gradient (Fig. 2d) and zonal advection of zonal momentum (Fig. 2c) combine to produce systematic eastward acceleration of the northward-moving ABL air. The meridional pressure gradient in Fig. 2f is strongest at the surface. Combined with the much weaker zonal advection of v (Fig. 2e), it accelerates ABL air to the north. In Fig. 3 the NCEP September–October mean surface pressure along 95°W (used to calculate the gradient at the surface in Fig. 2f) is compared to TAO surface pressure observations (triangles) for this period. Sampling is not continuous for the TAO moorings. We tried to compensate for sampling by interpolating the NCEP data to the location of the TAO buoys, and averaging the NCEP data only on those days in September and October when the TAO buoys reported surface pressure. This method results in little improvement in the agreement between the TAO and NCEP surface pressures, indicating that small discrepancies not related to sampling exist between the two datasets.

Mean vertical motion is an important forcing for boundary layer evolution. It is difficult to deduce from the type of in situ observations taken in EPIC 2001, so we turned to NCEP reanalysis. According to the September–October 2001 mean reanalysis, subsidence at 700 hPa in the region between 8°S and the equator was about 4 mm s^{-1}, and less to the north. This agrees with the rate of descent of plumes of moisture observed by the 3-hourly balloon soundings launched from the ship at 8°S (Bretherton et al. 2004). In our simulation, we specified a mean subsidence of $\hat{w} = -4$ mm s^{-1} above the relaxation height at all latitudes. Below z_{relax}, the subsidence linearly decreased to zero at the surface. We regard the decrease in NCEP subsidence north of the cold tongue to be due to occasional deep convection in the region. Since such deep convection is rarely seen south of 4°N, we felt it appropriate to use a subsidence rate consistent with radiative subsidence balance even north of the equator.

September–October 2001 mean NCEP reanalysis was used to provide the free-tropospheric winds and temperature as a function of latitude. Figure 4 shows the potential temperature, relative humidity, and zonal and meridional wind from September–October 2001 NCEP reanalysis from 8°S to 4°N. The temperature structure up through the ABL capping inversion is not well re-

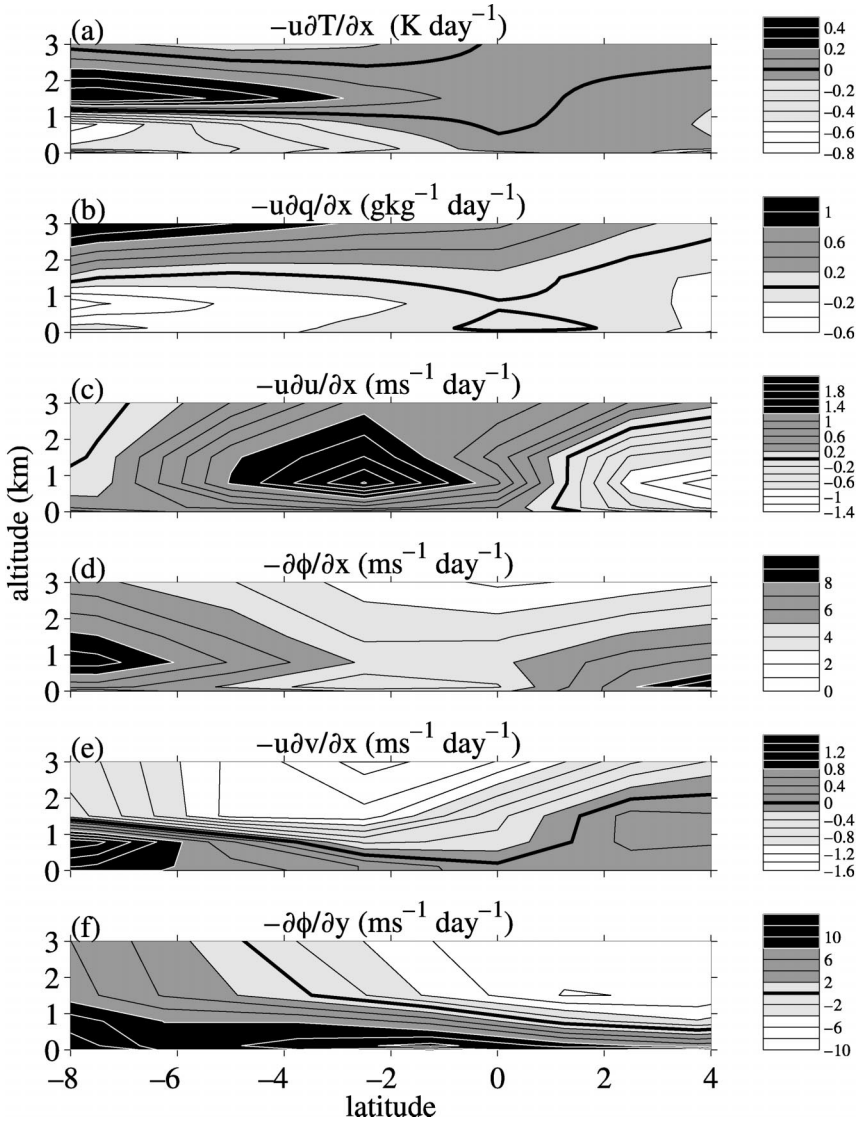

FIG. 2. Large-scale momentum forcings applied to the LES: Zonal advection of (a) temperature, (b) specific humidity, (c) zonal velocity, and (e) meridional velocity, together with (d) zonal and (f) meridional pressure gradient forces.

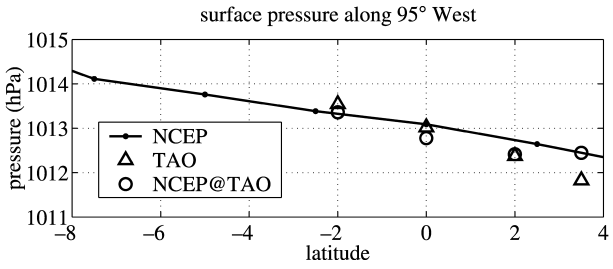

FIG. 3. The NCEP Sep–Oct mean sea level pressure along 95°W (black line), the average of all available TAO observations during the same period (triangles), and the average of NCEP data interpolated to TAO locations only when TAO data were available.

solved by the interpolated NCEP reanalysis data used here. For example, Fig. 5a compares the potential temperature sounding from the reanalysis to soundings from the *RHB* at 8°S. For a successful LES simulation, one must initialize with a realistic thermodynamic profile and maintain realistic free-tropospheric conditions at the relaxation level. Simply using the NCEP reanalysis to prescribe the free-tropospheric conditions would smear its coarsely resolved ABL into the free troposphere. To prevent this, we used the 600- and 700-hPa NCEP reanalysis levels to extrapolate winds and potential temperature down to the relaxation height.

The relative humidity observed on the EPIC 95°W flights was quite variable, and exceeded the NCEP relative humidity in the mean. We idealized the free-tropospheric relative humidity profile from the mean of the

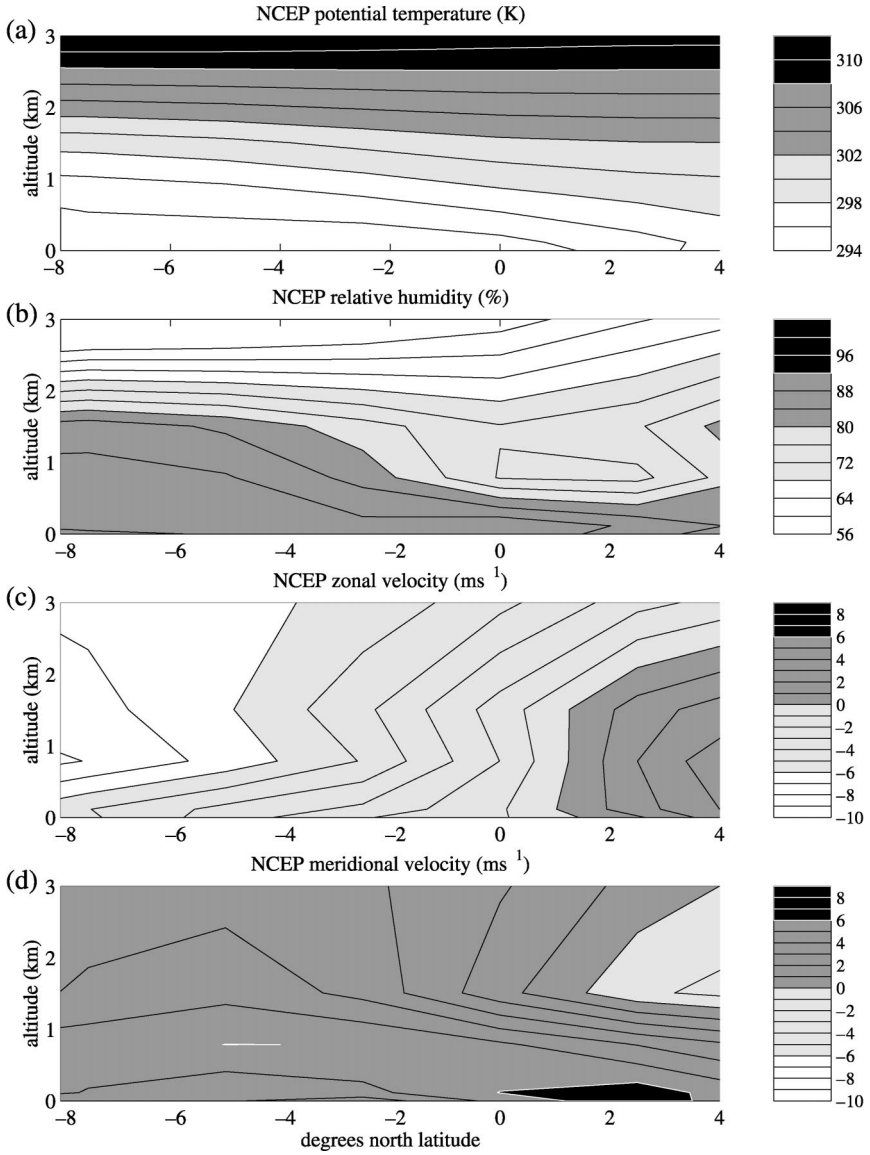

FIG. 4. Sep–Oct 2001 NCEP reanalysis cross section along 95°W, of (a) potential temperature, (b) relative humidity, (c) zonal velocity, and (d) meridional velocity.

EPIC 2001 dropsonde observations, excluding observations made in the boundary layer (see Fig. 8). Relative humidity south of the equator and above the ABL was linearly extrapolated using a relative humidity gradient of −3% per degree south. The cross sections of potential temperature, relative humidity and winds to which the LES simulations were relaxed above the boundary layer can be seen by looking above the inversion in the model results of Fig. 6.

For initialization, the simulation required vertical profiles of liquid water potential temperature θ_l, total water mixing ratio q_t, and wind $\mathbf{u}$ at the initial latitude of 8°S. Above the ABL, we initialized the LES with the potential temperature, relative humidity, and wind profiles used for the relaxation of the free troposphere at 8°S. The initial height of the ABL top and the initial thermodynamic profiles within the ABL were an idealized composite of three rawinsonde soundings, released from the *RHB* within 0.2° of 8°S. The thin black lines in Fig. 5 are the rawinsonde profiles, and the thick gray lines are the idealized profiles used to initialize the LES. Rawinsonde profiles from the *RHB* near 8°S were observed to jump from 10% to 80% relative humidity above the ABL in 3 h. The idealized profile, chosen to agree with NCEP reanalysis, was within the range of the observations. The initial wind profile was linearly interpolated from the NCEP reanalysis to the model levels and 8°S, 95°W.

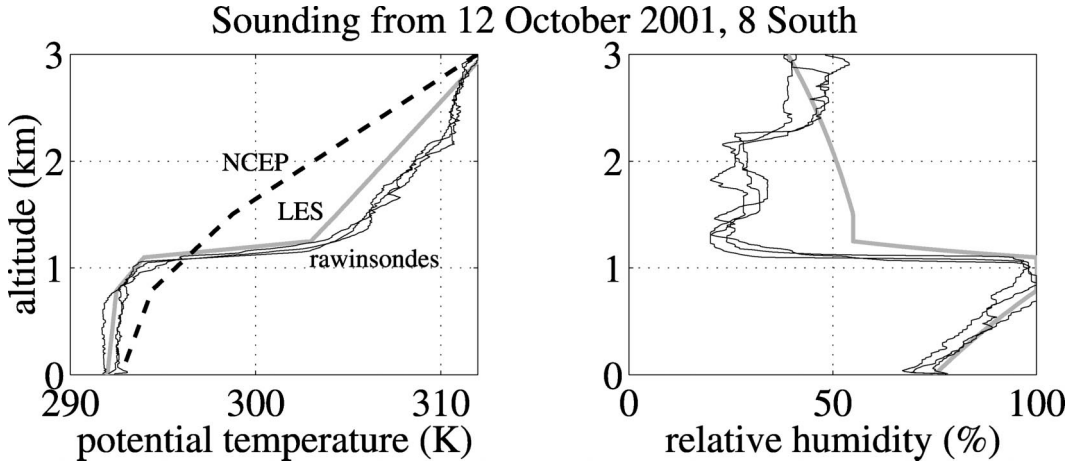

FIG. 5. (a) Potential temperature and (b) relative humidity from rawinsondes released from the *RHB* near 8°S on 12 Oct 2001 (thin black lines). For comparison, the dotted line is the NCEP reanalysis, and the gray line is the initial condition to the LES.

c. Large eddy simulation integration

The LES, called the Distributed Hydrodynamic Aerosol and Radiation Model Application (DHARMA), has a flux-limited, forward-in-time advection scheme (Stevens and Bretherton 1996). We ran DHARMA with periodic horizontal boundary conditions, using a domain size of 3.2 km × 3.2 km in the horizontal and 3 km in the vertical, and grid spacings of 50 m in the horizontal and 25 m in the vertical. This resolution required 64 × 64 × 120 grid points. Bretherton et al. (1999b) have shown 10-m vertical resolution reduces the overprediction of entrainment made by 25-m resolution simulations in radiatively driven stratocumulus. We chose 25-m resolution to accommodate the length of the integration, and expect the overprediction of entrainment to be less severe in the surface-driven ABL than in radiatively driven stratocumulus. The time step was adaptive, aiming to maintain a target maximum Courant number $\max_i(|u_i|\Delta t/\Delta x_i) = 0.5$, where the maximum was taken over the entire domain and all three velocity components u_i. The typical time step in our simulation was 3 s. DHARMA's parallel architecture allowed computations to be efficiently divided between multiple processors on a cluster of PCs. Using eight two-processor nodes, an integration of three model days at this resolution took about 5 days.

The surface fluxes were computed by the Coupled Ocean–Atmosphere Response Experiment (COARE) bulk flux algorithm (Fairall et al. 1996) from the properties of the lowest resolved grid point (12.5 m) and the SST. The idealized SST in Fig. 1 was assumed to be the skin temperature, so no additional skin temperature adjustments were applied. For the purposes of calculating the fluxes, the ocean surface current velocities were ignored.

Infrared and solar radiative fluxes were computed columnwise by BUGSrad (Stephens et al. 2001; Gabriel et al. 2001), an 18-band two-stream radiative transfer model developed for the Colorado State University GCM. Because of the computational expense of the radiation calculation, it was performed only every 20 time steps. Additionally, in each time step the radiation was calculated for any column where cloud appeared in a grid cell where it had not been the previous time step, or where cloud disappeared from a grid cell where it had been before. The downwelling solar flux, and the solar zenith angle at the top of the atmosphere were held constant. By reducing the solar constant by 1/2 to account for the fraction of daylight, and using the daylight-average cosine of the solar zenith angle (corresponding to a zenith angle of 51°), the constant solar flux used is equal to the expected diurnal-average of the solar flux at the top of the atmosphere. Above the LES domain, the radiative transfer code uses a standard tropical sounding of temperature and constituent concentrations.

DHARMA uses the bulk microphysical scheme of Wyant et al. (1997). Cloud liquid water q_c is diagnosed from q_t, θ_l, and ρ_0 assuming zero supersaturation. Total water q_t and liquid water potential temperature θ_l are not changed by condensation or evaporation of cloud water, so the only microphysical sources of q_t and θ_l are autoconversion and accretion of cloud water into rain water and evaporation of rain water. Autoconversion depends on q_c and a specified cloud droplet concentration, specified to be $N = 100\ \text{cm}^{-3}$. The vertical rain water flux is calculated by integrating the fall speed over the raindrop distribution. We use the subgrid-scale moist turbulence scheme of Wyant et al. (1997), based on Smagorinsky's (1963) first-moment closure.

3. Baseline case results

Figure 6 shows time–height cross sections of potential temperature, relative humidity, and wind components

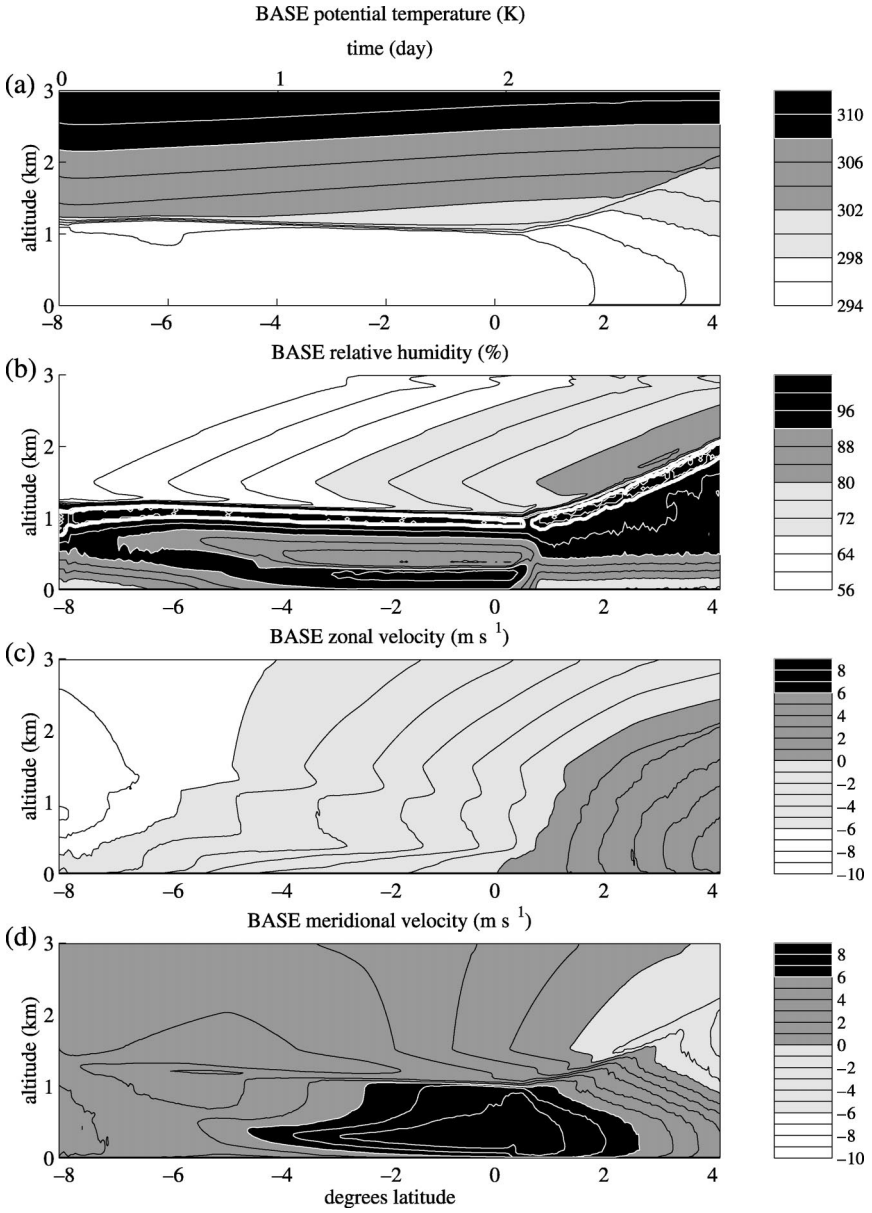

FIG. 6. Cross sections of the modeled cross-equatorial ABL from the BASE simulation. The shading and contour intervals are the same as in Fig. 4. The conditions above the ABL are relaxed to the NCEP reanalysis in Fig. 4. The 99.9% relative humidity contour, shown by the thick white contour in (b) is an approximate indicator of the presence of cloud.

for a baseline simulation (BASE) that uses the forcings and LES configuration described in section 2. The time axis (horizontally oriented in Fig. 6) can be interpreted equally well as latitude. We adopt this interpretation to facilitate comparison with the EPIC 2001 observations. BASE captures much of the observed ABL evolution along 95°W. The LES is not initialized with clouds, so there are transient adjustments from the formation of clouds in the first hours of model integration. After 3 h, when the column has traversed to about 7.5°S, the LES has completely spun up.

The modeled column simulates the two key transitions in the cross-equatorial ABL pointed out by WMD: the gradual formation of a stable layer over the equatorial cold tongue and the rapid transition to a cumulus-under-stratocumulus boundary layer over the warm SST. Cross sections of the simulated potential temperature, relative humidity, and wind in the same format as the NCEP cross sections in Fig. 4 are presented in Fig. 6. Between 8° and 6°S, the air–sea temperature difference is negative, so surface latent and sensible heat fluxes provide ample moisture for the clouds. As the column

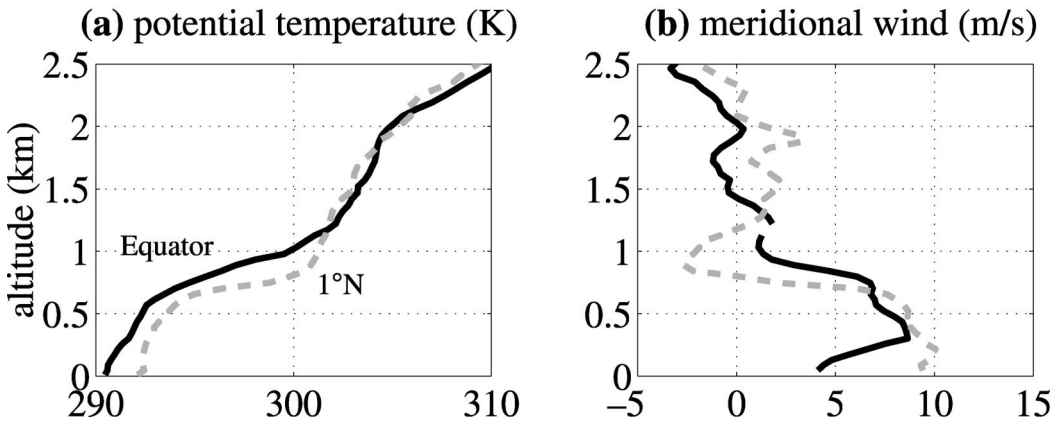

FIG. 7. Potential temperature and meridional wind observations from dropsondes released during research flight 3 show wind shear in the lower 300 m in the stable region over the equator (black). At 1°N, the potential temperature and momentum are mixed throughout the ABL (gray dashed).

goes north from 6°S to the equator over progressively cooler SST, the inversion lowers a little, and the cloud thins. The entrainment rate is $w_e = 3$ mm s^{-1}, a little weaker than the subsidence $\hat{w} = -4$ mm s^{-1}. Over the coldest water, a stably stratified shear layer in both wind components forms within the ABL near the surface due to the surface stability. Figure 7 shows profiles of potential temperature and meridional wind at the equator and 1°N, 95°W measured by dropsondes released from the C-130 aircraft during EPIC 2001. The equatorial sounding shows the stability and wind shear in the lowest 300 m. Inefficient turbulent mixing within this layer leads to weak surface winds and greatly reduced surface fluxes.

Starved of surface moisture flux, the modeled stratocumulus cloud nevertheless persists over the cold tongue, maintaining a delicate balance at the cloud top between radiative cooling and entrainment warming. A second transition takes place rapidly after the column crosses the warm SST front. As suggested by WMD, over positive sensible and latent surface heat flux, the surface stable layer is mixed out and the near-surface winds increase again. In this convective ABL, cumulus rising into stratocumulus clouds impinge on the inversion and rapidly deepen the boundary layer by entrainment. The inversion rises at a rate of 1.3 cm s^{-1}, implying an entrainment rate of $w_e = 1.7$ cm s^{-1}. This is larger, but in qualitative agreement with estimates of entrainment from heat and mass budgets derived from the EPIC 2001 observations along 95°W (de Szoeke et al. 2004, manuscript submitted to *J. Atmos. Sci.*) and from coarse-scale observations of downstream deepening of the boundary layer (Wood and Bretherton 2004).

For comparison, Fig. 8 shows composite cross sections of the atmosphere observed during EPIC 2001 between 8°S and 4°N along 95°W using all available in situ measurements. Between 8°S and 2°S, these are derived from rawinsondes released from a single transect of the *RHB*. Farther north we use an eight-flight mean of in situ observations from the C-130 (1°S–4°N below 1600 m), and dropsondes from the C-130 (0°S–4°N above 1600 m). The boundary layer capping inversion (the stable layer near 1000 m in Fig. 7a) rises slightly and weakens in stability from the equator to 4°N. The cross sections of potential temperature for individual flights (not shown) resolve the inversion better than the mean, because the averaging tends to blur the sharp features sampled on each flight. The mean relative humidity cross section in Fig. 7b shows a wedge of high-humidity air widening between 1° and 4°N. This widening wedge of relative humidity is the conflated signal of the rising boundary layer top and the moist air above the ABL that has episodically been advected to these latitudes from the north and east. Though model results in Fig. 6 do not predict all the features of the observations presented in Fig. 7, the major features agree acceptably. The largest shortcoming of the simulation is the unrealistically large entrainment rate north of the equator. This could be partly due to the very moist free troposphere prescribed in the northern part of the simulation. Both modeled (Fig. 6d) and observed (Fig. 7d) meridional wind exhibit a wind minimum at the surface and a roughly 400–600-m-high jet from 5°S to the equator. North of the SST front, at about 0.5°N, the modeled and observed meridional wind jet spreads downward to the surface.

Figure 9 compares the modeled and observed surface sea and air temperature. The observations were taken from the separate *RHB* ship transects, one north and one south of 1°S, and from the September–October means measured by TAO buoys. The ABL experiences large gradients of SST as it advects northward. Where the SST is cooling as the air moves northward, the advection of warm air over cooler water leads to a stabilization of the lower boundary layer. Between 4°S and the equator, the modeled surface air temperature is 0.5°C warmer than the SST. This air–sea temperature difference has the opposite sign from the ship observations for reasons

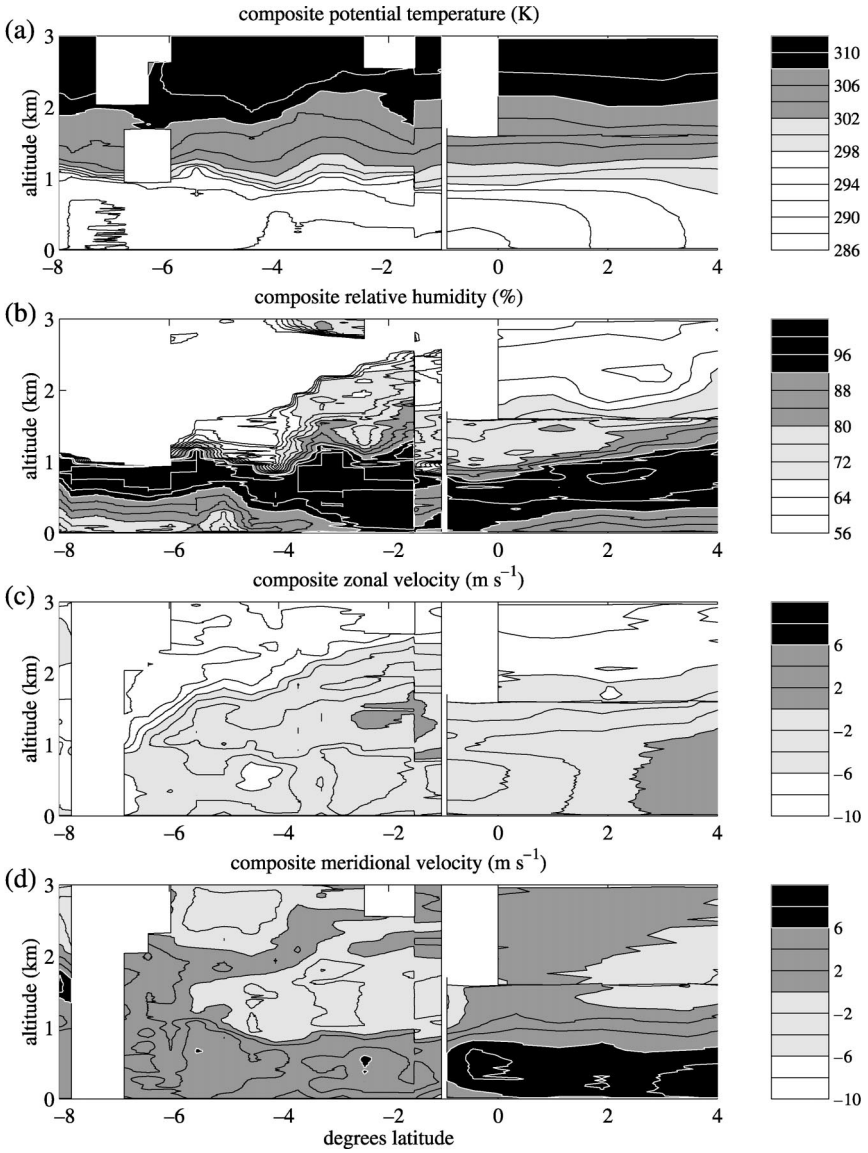

FIG. 8. Cross sections at 95°W composited from the EPIC 2001 observations. Profiles between 1° and 8°S are from rawinsondes released from the *RHB*. Profiles north of 1°S and below 1600 m are measured in situ by the C-130 aircraft. North of the equator and above 1600 m, the profiles are from dropsondes dropped by the C-130. Axes, contours, and shading are as in Fig. 4.

we do not fully understand. While aircraft observations showed the lower ABL usually to be slightly stably stratified at the equator during EPIC 2001, positive air–sea temperature differences were rarely observed either by the TAO buoys or the ship. The warmer air temperature seen in the model between 5°S and the equator would be reduced by the effect of differential advection. Slower advection of the layer near the surface would give it more time to cool as it passes over the decreasing SST. This effect alone cannot explain the observed negative air–sea temperature difference, however. Radiative cooling must be strong and entrainment warming must be weak to account for the cold air temperatures. Over the warmer SST north of the equator, where the air is still cool, the air–sea temperature difference is more than −3°C in the model and in situ observations, and strong positive surface heat fluxes drive boundary layer convection. At the equator, the TAO buoys are often slightly north of the SST front; this is reflected in both the SST and the surface air temperature.

The quasi-Lagrangian method is based on the assumption that the advection velocity, in this case the NCEP 1000–925-hPa meridional wind, is representative of the ABL-mean velocity. As a test of the consistency of the quasi-Lagrangian method in this case, we compare the ABL-mean meridional velocity V as defined in

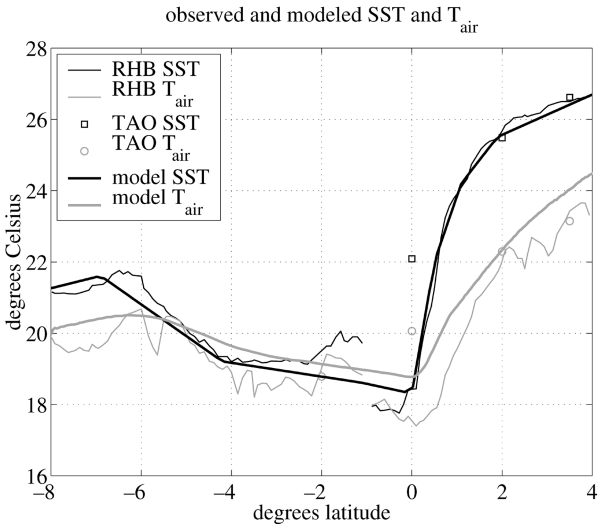

FIG. 9. The SST prescribed to the LES is an idealization of the observed SST (black lines). The modeled 12.5-m air temperature is compared with TAO and *RHB* surface air temperatures (gray lines).

(11) to the NCEP 1000–925-hPa meridional wind in Fig. 10. Relative to NCEP, the LES ABL experiences more fluctuation in *V*, though *V* is comparable to NCEP when averaged over the entire integration. A possible explanation is that the prescribed pressure gradient derived from the NCEP reanalysis is too smooth to locally balance the surface and entrainment drag, which are driven by small-scale changes in SST.

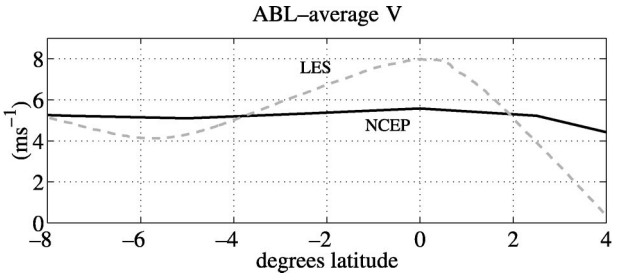

FIG. 10. NCEP 1000–925-hPa wind (solid) compared to the ABL-mean meridional wind from the LES (dashed).

The thermodynamic evolution of the ABL was nearly unaltered by changing the advective meridional wind speed. In a simulation in which the prescribed advective velocity and pressure gradients were increased corresponding to two standard deviations of the August–November 1000-hPa meridional wind, the stronger pressure gradients drove higher winds and stronger fluxes. However, the fluxes' effects were mitigated by the larger advective velocity.

a. The influence of stability on the ABL momentum

As pointed out by WMD, the effect of the near-surface stratification can be seen in the observed surface wind field. In Figs. 11b,c, we compare our modeled surface (12.5 m) winds with 30 September–2 October 2001 average 95°W 10-m winds derived from the Sea Winds

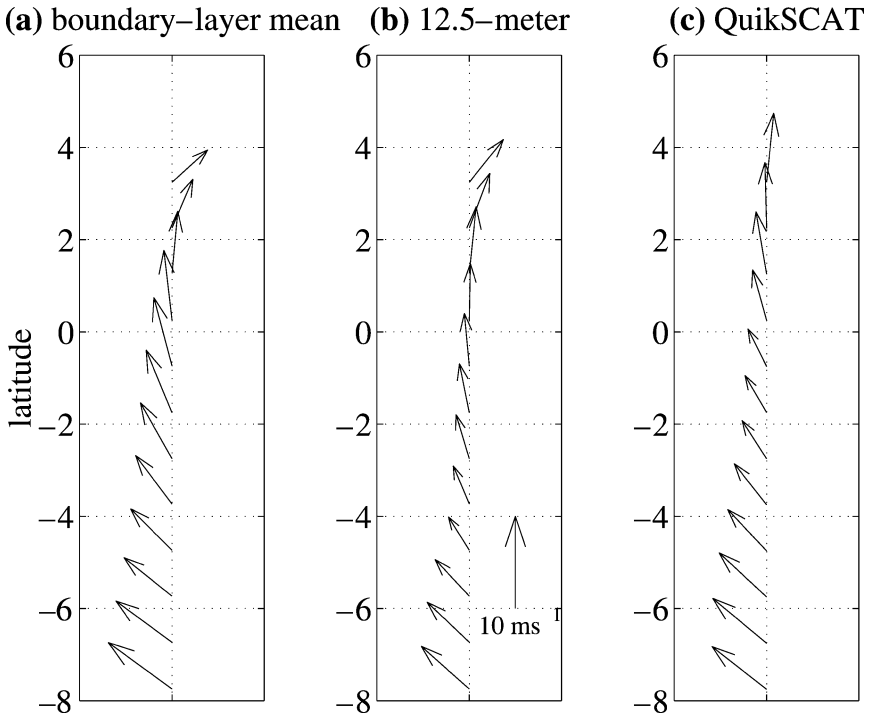

FIG. 11. The (a) ABL-average and (b) surface (12.5 m) wind modeled by BASE, compared to (c) 30 Sep–2 Oct 2001 average QuikSCAT observations.

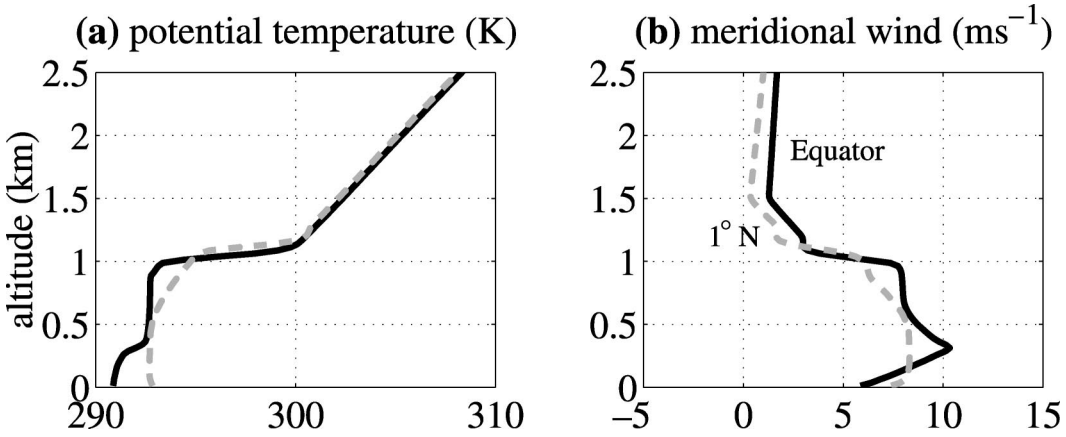

FIG. 12. Modeled soundings of (a) potential temperature and (b) meridional wind over the equator (black) and 1°N (gray dashed) (cf. observations in Fig. 8).

microwave scatterometer on the QuikSCAT satellite, provided by D. Chelton. Both the QuikSCAT and the modeled winds show 6–8 m s^{-1} southeasterlies at 8°S, lower surface winds of about 4 m s^{-1} over the cold SST region from 5°S to the equator, and rapid acceleration of the surface winds north of the equator. The LES shows more extreme surface wind decrease than QuikSCAT, perhaps due to its excessive near-surface layer stability, but the modeled near-surface shear is not an artifact. The jet at 400–600 m and reduced surface wind speed was seen by Bond (1992), Yin and Albrect (2000), and Zeng et al. (2004) from soundings released from ships, by the NOAA Galapagos wind profiler, and by McGauley et al. (2004, hereafter MZB) from EPIC 2001 aircraft in situ and dropsonde observations. The modeled ABL-average wind (Fig. 11a) shows that the surface wind speed changes are not seen throughout the depth of the ABL, indicating that remixing of momentum within the ABL is responsible for much of the surface wind change across the equator, consistent with WMD. The clockwise turning of the wind with latitude north of the equator is stronger in the LES than in the QuikSCAT observations, probably reflecting differences between the pressure gradients prescribed to the model, and the true pressure gradients on these days. The 3-day average of QuikSCAT observations is good for comparison with the LES because it preserves the sharpness of the SST front, but it is not necessarily climatologically representative.

LES profiles of the potential temperature and meridional wind (Fig. 12) show the link between near-surface stability and shear. The black lines represent profiles at the equator, over cold SST, and the gray dashed lines represent profiles at 1°N, over warm SST. The modeled profiles at the equator show a stably stratified shear layer capped by a maximum in the meridional wind at about 300 m. Over the 0–300-m layer, the bulk Richardson number is 0.6, but below 200 m the atmosphere is less statically stable, and the local Richardson number is 1/3, the threshold for subgrid-scale diffusion in the LES. Subgrid diffusion mixes the potential temperature in this layer, maintaining its low static stability. It is important to note that with the grid resolution used in BASE there are almost no grid-resolved eddy motions in this shear layer. The LES is acting as an expensive single-column model relying primarily on its subgrid diffusion scheme. In this regime, much finer spatial grid resolution would be needed for a truly eddy-resolving simulation of this shear layer.

While aircraft observations during EPIC did not go farther than 1°S, the model shows acceleration of the meridional wind near 500 m from 5°S to the SST front at 0.5°N (see Fig. 6). The surface drag is not transmitted above the internal stable layer, so the pressure gradient accelerates the wind, unhindered by friction. Here, over the cold water, where the internal stable layer could be said to lubricate the middle ABL from surface friction, the ABL coupling to the surface is ''slippery.'' The imposed meridional pressure gradient decreases with altitude over the cold tongue, contributing an acceleration term of up to 10 m s^{-1} day^{-1} near the surface, and vanishing at about 1 km. This explains why the simulated wind maximum is at or below the middle of the ABL.

The gray dashed line in Fig. 12 shows the profile of potential temperature and meridional wind at 1°N, where over the previous hours, the ABL column has traversed some 50 km over an unstable air–sea temperature difference. Vigorous convection has created a well-mixed layer up to 500 m in both potential temperature and meridional wind. The surface wind speed is larger than at the equator as a result of downward mixing. Here the ABL–surface coupling is ''sticky'' because surface friction is transmitted throughout the lower ABL.

The rapidity of the transition is illustrated in Fig. 13, which is a cross section of the BASE simulation over a 6-h period as the column passes over the SST front. Because of the initial surface stability, the air temperature responds slowly to the SST increase. When the SST reaches 1°C warmer than the air temperature at

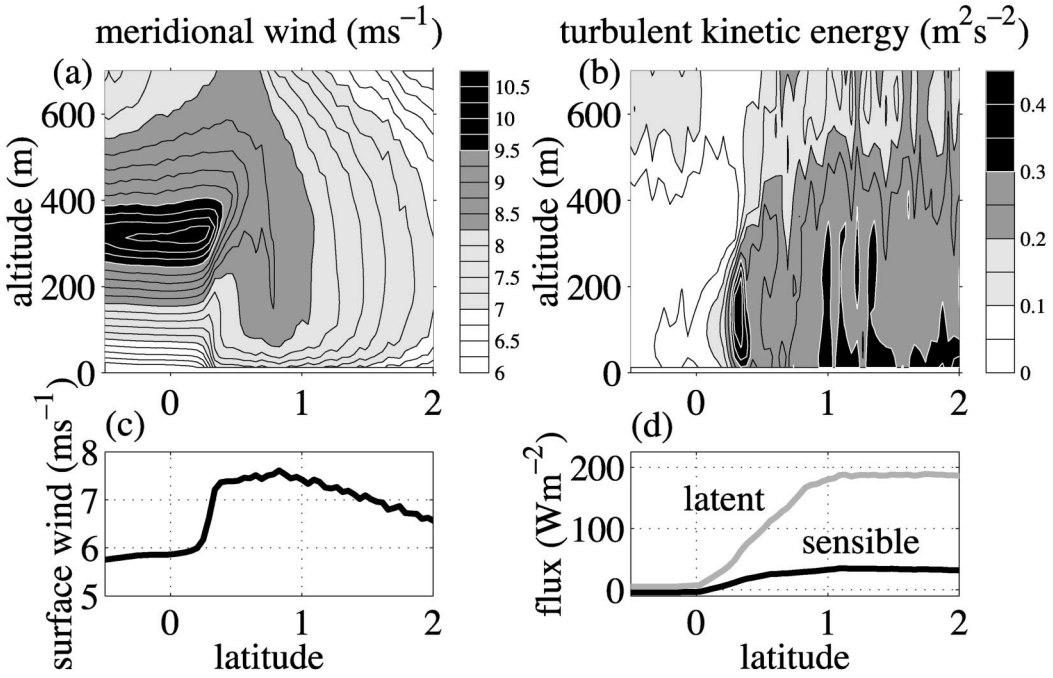

FIG. 13. The transition of the lower ABL as the ABL crosses the SST front in simulation BASE.

about 0.3°N the atmosphere responds with buoyant convection near the surface, generating substantial resolved-scale turbulent kinetic energy (Fig. 13b). The convection mixes the potential temperature and momentum (Fig. 13a). The mixing is so fast in BASE that the surface wind adjusts by increasing 1.5 m s^{-1} in 1 h (Fig. 13c). After the initial adjustment, the wind is relatively steady, but the surface fluxes (Fig. 13d) continue to increase because the SST–air temperature difference is still rising. The surface meridional wind slowly decreases north of 1°N due to mixing of lower-momentum air from aloft, continued surface drag, and the eastward turning influence of Coriolis force.

b. Momentum budget

To compute the momentum budget for the ABL, we first define the average velocity in the ABL:

$$\mathbf{U} = \frac{1}{M}\int_0^{z_{\text{int}}} \rho_0 \overline{\mathbf{u}}\, dz = \langle \overline{\mathbf{u}} \rangle, \tag{11}$$

where the overbar denotes the horizontal average **u**, the angle brackets $\langle\ \rangle$ denote the density-weighted vertical average, and

$$M = \int_0^{z_{\text{int}}} \rho_0\, dz \tag{12}$$

is the column mass per unit area of the ABL. For the purpose of computing the budget, we define a horizontal ABL-top interface to be 75 m above the mean inversion height, $z_{\text{int}} = \overline{z_{\text{inv}}} + 75$ m. Integrating from the surface to z_{int} ensures that we account for all the cloud-top radiative flux, even if there is variability in the cloud-top height, but that we do not count the relaxation sources in the free troposphere ($z_{\text{relax}} = \overline{z_{\text{inv}}} + 150$ m). Differentiating (11) with respect to time yields

$$\frac{d\mathbf{U}}{dt} = \left\langle \frac{\partial \overline{\mathbf{u}}}{\partial t} \right\rangle + \frac{\rho_0(z_{\text{int}})}{M}[\overline{\mathbf{u}}(z_{\text{int}}) - \mathbf{U}]\frac{dz_{\text{int}}}{dt}. \tag{13}$$

The first term in this derivative is the mass-weighted vertical integral of the derivative of the horizontally averaged velocity $\overline{\mathbf{u}}$, the second is the effect of incorporating air with velocity $\overline{\mathbf{u}}(z_{\text{int}})$ into the ABL. Combining the horizontal average of the momentum equation (1) with (13), using the anelastic continuity equation (5), and then rearranging the terms, we obtain the following ABL-averaged momentum budget equation:

$$\frac{d\mathbf{U}}{dt} = -\langle f\mathbf{k} \times \overline{\mathbf{u}} \rangle - \left\langle \hat{u}\frac{\partial \hat{\mathbf{u}}}{\partial x} + \boldsymbol{\nabla}\hat{\phi} \right\rangle + \frac{1}{M}\overline{\mathbf{F}}^{\mathbf{u}}_{\text{sfc}} + \mathbf{A}_{\text{entr}}, \tag{14}$$

where

$$\mathbf{A}_{\text{entr}} = \frac{\rho_0(z_{\text{int}})}{M}\left\{ -\overline{\mathbf{u}'w'}(z_{\text{int}}) - \overline{\mathbf{F}}^{\mathbf{u}}_{\text{sgs}}(z_{\text{int}}) + [\overline{\mathbf{u}}(z_{\text{int}}) - \mathbf{U}]\frac{dz_{\text{int}}}{dt} \right\} - \left\langle \hat{w}\frac{\partial \overline{\mathbf{u}}}{\partial z} \right\rangle. \tag{15}$$

The vertically averaged ABL accelerations are Coriolis acceleration, large-scale horizontal accelerations (zonal

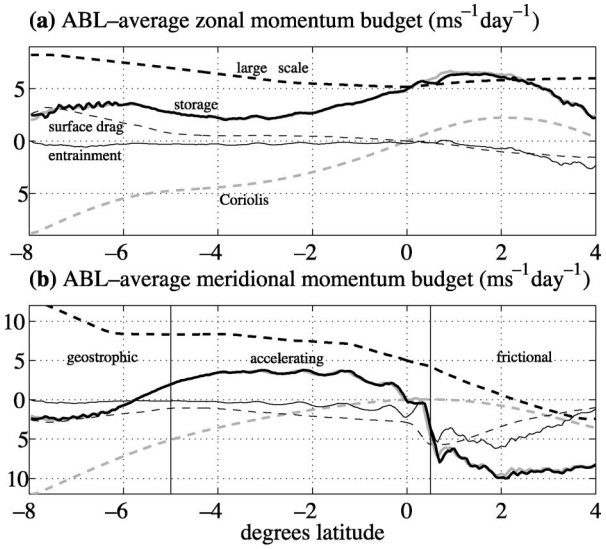

FIG. 14. The (a) zonal and (b) meridional components of the momentum budget (14). The accelerations (labeled on the zonal budget) are ''large scale'' (pressure gradients and zonal advection) (dashed), ''Coriolis'' (gray dashed), ''surface drag'' (thin dashed), and ''entrainment'' (thin). The storage (black) balances the sum of the forces (solid gray) within small discretization errors. The labels on the meridional budget refer to the three different flow regimes discussed in the text.

advection and pressure gradient accelerations), surface drag $\overline{\mathbf{F}}^{\mathbf{u}}_{\text{sfc}}$, and entrainment acceleration. The entrainment acceleration includes turbulent flux at the ABL-top interface $\overline{\mathbf{u}'w'}(z_{\text{int}})$ and subgrid-scale entrainment flux $\overline{\mathbf{F}}^{\mathbf{u}}_{\text{sgs}}(z_{\text{int}})$ (both usually small), the term from (13) due to the rising inversion, and the subsidence. Large-scale advection due to subsidence is combined into the entrainment term because it contributes a momentum flux through the ABL top.

Figure 14 shows the ABL zonal and meridional momentum budgets. The sum of the accelerations is compared with the ''storage'' $d\mathbf{U}/dt$. The storage of the mean momentum and the tendency of the inversion height are computed with centered time differencing. The instantaneous budget terms, computed every 15 min of model integration, are noisy due to sampling, so we have low-pass-filtered the terms shown in Fig. 14 with a 2-h running mean. With or without filtering, there is excellent agreement between the sum of the accelerations on the right-hand side of (14) and the storage $d\mathbf{U}/dt$.

The meridional budget shows the transition from a situation where the mean-ABL meridional momentum is relatively unaffected by surface and entrainment drag over cold SST, to one where friction dominates the balance of forces over warm SST. South of 5°S, the dominant balance is between the Coriolis force and the ''large-scale'' force. Since the large-scale force in this region is 90% meridional pressure gradient, and only 10% zonal advection, this balance is essentially geostrophic. Between 5°S and the warm SST front at 0.5°N, the Coriolis force is too small to balance the large-scale pressure gradient, and the ABL flow accelerates due to the pressure gradient unchecked by any other significant force. North of 0.5°N, vigorous convection enhances both surface drag and turbulent entrainment of slower-moving air into the boundary layer from above. In this region, surface drag and entrainment each contribute about 5 m s^{-1} day^{-1} of meridional ABL deceleration. Both terms weaken farther north. The surface drag weakens due to the decreased meridional wind component. The entrainment weakens because vertical wind shear decreases in association with mixing of momentum through a deeper layer by shallow convection.

In the zonal momentum budget, the wind is accelerating eastward everywhere, mostly due to a ubiquitous eastward large-scale acceleration that exceeds the Coriolis force north of 4°S. This large-scale acceleration is about 80% pressure gradient and 20% zonal advection. Both entrainment and surface drag slightly reduce the eastward acceleration over the warm water.

Simplified models have been used to model the steady cross-equatorial flow. Tomas et al. (1999) showed that meridional advection of negative absolute vorticity predicted the northward displacement of the intertropical conversion zone (ITCZ) from the equator. By prescribing the meridional trajectory to our LES, we assume a steady state, and attribute the modeled momentum tendency to advection by the prescribed wind. Since the tendency in Fig. 14 is not small compared to the other forcings, our LES results support the importance of meridional advection to the momentum budgets.

Stevens et al. (2002) propose a model of tropical surface winds in which they consider a well-mixed ABL, neglect nonlinear advection in the ABL, but include a simple formulation for entrainment of free tropospheric air into the ABL. Figure 2 implies that in the EPIC region, neglect of nonlinear advection is justifiable for zonal advection (at least to leading order) but Fig. 14 suggests the meridional advection (the storage term) is not negligible. South of the equator, entrainment is small and the ABL is not well mixed, so the constant entrainment used in the Stevens et al. model is not expected to be realistic there. North of the equator, there is a 500-m layer fairly well mixed in momentum and there is considerable entrainment deceleration of the ABL, qualitatively consistent with the idealizations of Stevens et al. The results of Stevens et al. are quantitatively tested against EPIC 2001 observations by MZB.

c. *The equilibrium of thin clouds and the ABL heat budget*

The modeled clouds over the cold tongue are surprisingly persistent, despite a lack of surface heat and moisture fluxes to maintain them. One reason is that unlike almost anywhere else outside the Arctic, the specific humidity above the eastern equatorial ABL tends to be as large or larger than within the ABL. This means that the cloud is susceptible to warming from entrain-

ment, but not to drying. In Fig. 6b, the stratocumulus cloud over the cold tongue is a little thicker than 100 m. The cloud top lowers 160 m as the column moves from 6°S to the equator, which is only 25% of the time-integrated large-scale subsidence during this time. This implies that the entrainment rate must be $w_e = 3$ mm s^{-1}, 75% as large as the specified subsidence rate $\hat{w} = -4$ mm s^{-1}. The entrainment is sustained by weak turbulence in the upper ABL, driven by radiative cooling of 2 K h^{-1} at the top two grid points of the cloud. Entrainment warming alone tends to thin the cloud, but the radiative cooling compensates to allow a thin cloud layer to be sustained. Thus, in the absence of any other cooling of the cloud layer, cloud-top radiative cooling is important for maintenance of clouds over the cold tongue.

We can quantify these processes more systematically with an ABL-integrated heat budget, formulated in terms of liquid water potential temperature θ_l to avoid the complication of the condensation term. The budget is obtained similarly to the momentum budget (14). We horizontally average (2) to obtain $d\overline{\theta}_l/dt$; multiply by the base-state density ρ_0, the specific heat of air C_P, and the base state Exner function Π_0 (all of which are time invariant); then integrate from the surface to the inversion z_{int}. The result can be manipulated:

$$C_P\langle\Pi_0\rangle M\frac{d}{dt}\Theta = \overline{F}^{\theta_l}_{\text{sfc}} - (\overline{F}_{\text{rad}})_0^{z_{\text{int}}} + \rho_0 L\overline{F}_{\text{pcp}}(0) + M\langle C_P\Pi_0\overline{S}^{\theta_l}_{\text{LS}}\rangle + M\langle C_P\Pi_0\overline{S}^{\theta_l}_{\text{other}}\rangle + \overline{F}_{\text{entr}}, \tag{16}$$

where

$$\overline{F}_{\text{entr}} = (\rho_0 C_P\Pi_0)_{z_{\text{int}}}\left\{[\overline{\theta}_l(z_{\text{int}}) - \Theta]\frac{dz_{\text{int}}}{dt} + \overline{w'\theta_l'}(z_{\text{int}})\right\} - \left\langle\rho_0 C_P\Pi_0\hat{w}\frac{\partial\overline{\theta}_l}{\partial z}\right\rangle, \quad \text{and} \tag{17}$$

$$\Theta = \frac{\langle\Pi_0\overline{\theta}_l\rangle}{\langle\Pi_0\rangle} \tag{18}$$

is the ABL average θ_l, weighted by the base-state density and Exner function $\rho_0\Pi_0$. The terms on the right-hand side of (16) are the surface flux $\overline{F}_{\text{sfc}}$; the radiative flux convergence into the ABL $[\overline{F}_{\text{rad}}]_0^{z_{\text{int}}}$; the net ABL latent heating $\rho_0 L\overline{F}_{\text{pcp}}(0)$, which is proportional to precipitation reaching the surface; the large-scale advective forcing $S^{\theta_l}_{\text{LS}}$; and other θ_l sources $\overline{S}^{\theta_l}_{\text{other}}$, the largest of which is the subgrid-scale flux convergence, whose effect is small when integrated over the ABL. The entrainment heat flux $\overline{F}_{\text{entr}}$ includes the effect of changing the inversion height, which incorporates air with liquid water potential temperature $\overline{\theta}_l(z_{\text{int}})$ in excess of the ABL-average liquid water potential temperature Θ, as well as resolved turbulent and subsidence flux through the ABL-top interface.

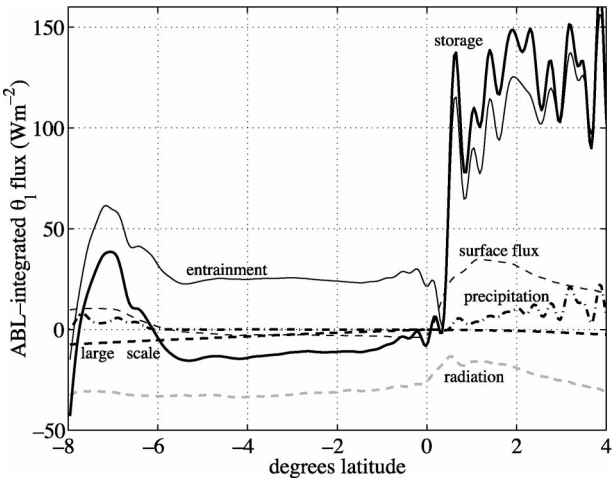

FIG. 15. Terms in the ABL vertically integrated θ_l budget (16): radiation (gray dashed), entrainment (black thin), surface flux (thin dashed), storage (black), large-scale advection (black dashed), and precipitation (black dotted–dashed).

Figure 15 shows how the heat budget terms depend on latitude in BASE. Our diagnosis of z_{inv} (and hence z_{int}) tends to ''stair step'' between model grid layer interfaces, especially in the weak turbulence regime from 0°–4°S. This introduces spurious oscillations in dz_{int}/dt. To remove this undesirable stepping feature we found the intersection times z_{inv} with the grid interfaces, and used cubic spline interpolation to get $z_{\text{inv}}(t)$ between these intersection times. For clarity, we filtered all the terms with a 2-h low-pass Butterworth filter. With or without filtering, the terms on the right-hand side of (16) add up to the ABL mean tendency to high accuracy as they should.

Over the cold tongue between 6°S and 0°S, the dominant balance is between radiative cooling and entrainment warming, each exceeding 30 W m^{-2}. Zonal advection and surface heat flux each contribute up to 3 W m^{-2} of cooling. The sum of the heating terms nearly cancel, so that the mean θ_l of the ABL cools only slightly over the cold tongue. North of the warm front, the entrainment flux is responsible for most of the warming; surface flux is also significant. These overwhelm the radiative flux divergence to produce rapid ABL heating, seen by the large storage term. As the clouds thicken, ABL latent heating due to precipitation also becomes noticeable.

4. Sensitivity studies

To explore some ABL feedbacks due to particular physical processes, and to test the effect of model resolution, we performed several sensitivity studies, summarized in Table 1. First, we ran the model for a case with half the domain size in both horizontal dimensions (HALF). We ran three cases with some of the physical forcings turned off: with no cloud radiative forcing

TABLE 1. Abbreviations and descriptions for each simulation.

Case name	Description
BASE	3.2 km × 3.2 km domain size baseline EPIC 2001 cross-equatorial flow simulation
HALF	1.6 km × 1.6 km simulation otherwise like BASE (all remaining cases are 1.6 km × 1.6 km)
NOCRF	Cloud radiative forcing turned off
NOZONADV	Large-scale zonal advection turned off
NODRIZ	Precipitation turned off
IQM1	Initial ABL q_t reduced by 1 g kg^{-1}
IQM2	Initial ABL q_t reduced by 2 g kg^{-1}
DRY	Above-ABL free-troposphere relative humidity reduced by 40%
MIDNIGHT	Diurnally varying solar flux, initialized at local midnight
NOON	Diurnally varying solar flux, initialized at local noon

(NOCRF), with no zonal advection (NOZONADV), and with no drizzle (NODRIZ). We ran two cases with the initial specific humidity reduced to look at the impact of the initial sounding on the clouds (IQM1 and IQM2). During EPIC 2001, significant variability was observed in the humidity above the boundary layer. This was investigated in case DRY. Cases MIDNIGHT and NOON explore feedbacks associated with the diurnal cycle of insolation.

a. Domain size

In the case HALF, the horizontal length and width of the domain were halved, to 1.6 km each. The resolution was kept the same, so the number of horizontal grid points went from 64 × 64 to 32 × 32, totaling one-fourth of the original number of horizontal grid points. The domain height (3 km) and resolution (120 points) were unchanged.

Reducing the number of grid points and the domain size has almost no effect on the horizontally averaged fields throughout the simulation (cf. Fig. 16a with Fig. 6b). The most noticeable difference of HALF from BASE is that the cumuliform convection that underlies the stratocumulus in the region north of the equator is more episodic for the smaller domain, which is too small to support even a single steady cumulus updraft.

Because of the insignificant effect of reducing the domain size, we infer that while the baseline 3.2 km × 3.2 km domain size is better for representing the ABL large eddy structure, the smaller domain size—requiring only 25% of the computer time of BASE—is sufficient for further sensitivity studies.

b. The influence of physical model forcings

Cloud radiative feedback, large-scale advection, and precipitation all influence the simulated ABL. To isolate their effects, we ran the model with the 1.6 km × 1.6 km domain three times, each time with one of the three forcings turned off.

1) CLOUD RADIATION

Cloud radiative forcing (CRF) cools the top of the cloud layer. Radiative cooling drives cloud-top convective downdrafts, and causes turbulent entrainment. Over the cold tongue, where no buoyancy flux is provided at the surface, radiatively driven entrainment maintains the height of the boundary layer against subsidence. In section 3c we hypothesized that CRF is a crucial process in maintaining clouds over the cold tongue. To test this, we performed a simulation (NOCRF) with CRF removed by input of zero liquid water to the radiative transfer scheme. The cloud fraction from NOCRF is shown in Fig. 16b.

The height of the inversion can be judged from the cloud tops in Fig. 16. Switching off the CRF greatly reduces the entrainment compared to HALF. For cases BASE and HALF, the inversion descends 200 m between 8°S and the equatorial SST front, and the corresponding time-averaged entrainment velocity is 2.9 mm s^{-1}. For NOCRF, the inversion descends 700 m, and the entrainment velocity is only 0.3 mm s^{-1}. In the surface-driven regime north of the warm front, entrainment velocities for the two cases in this region are almost identical.

With no CRF, the inversion drops below the lifting condensation level and the clouds evaporate between 4° and 5°S. As the ABL continues to shallow (to as low as 500 m) without entrainment, the relative humidity increases in the ABL. Clouds form at the top of this shallow layer between 3°S and the warm front. North of the warm front, both the cloud fraction and ABL height remain lower than in HALF.

2) PRECIPITATION

As seen in Fig. 15, significant precipitation occurs only at latitudes north of the SST front, where the stratocumulus cloud is thickest. Over the cold tongue, there is no moisture source, and clouds are too thin to drizzle. To see the effect of precipitation on the ABL evolution, we performed a simulation NODRIZ with the precipitation microphysics turned off.

Comparing HALF (Fig. 16a) and NODRIZ (Fig. 16c), drizzle thins the cloud where it would be thickest—between 8°–6°S and over the warm-SST regions, where the surface latent heat flux is large. In NODRIZ, the stratocumulus cloud south of the equator thickens somewhat compared to HALF. Surprisingly the cloud fed by

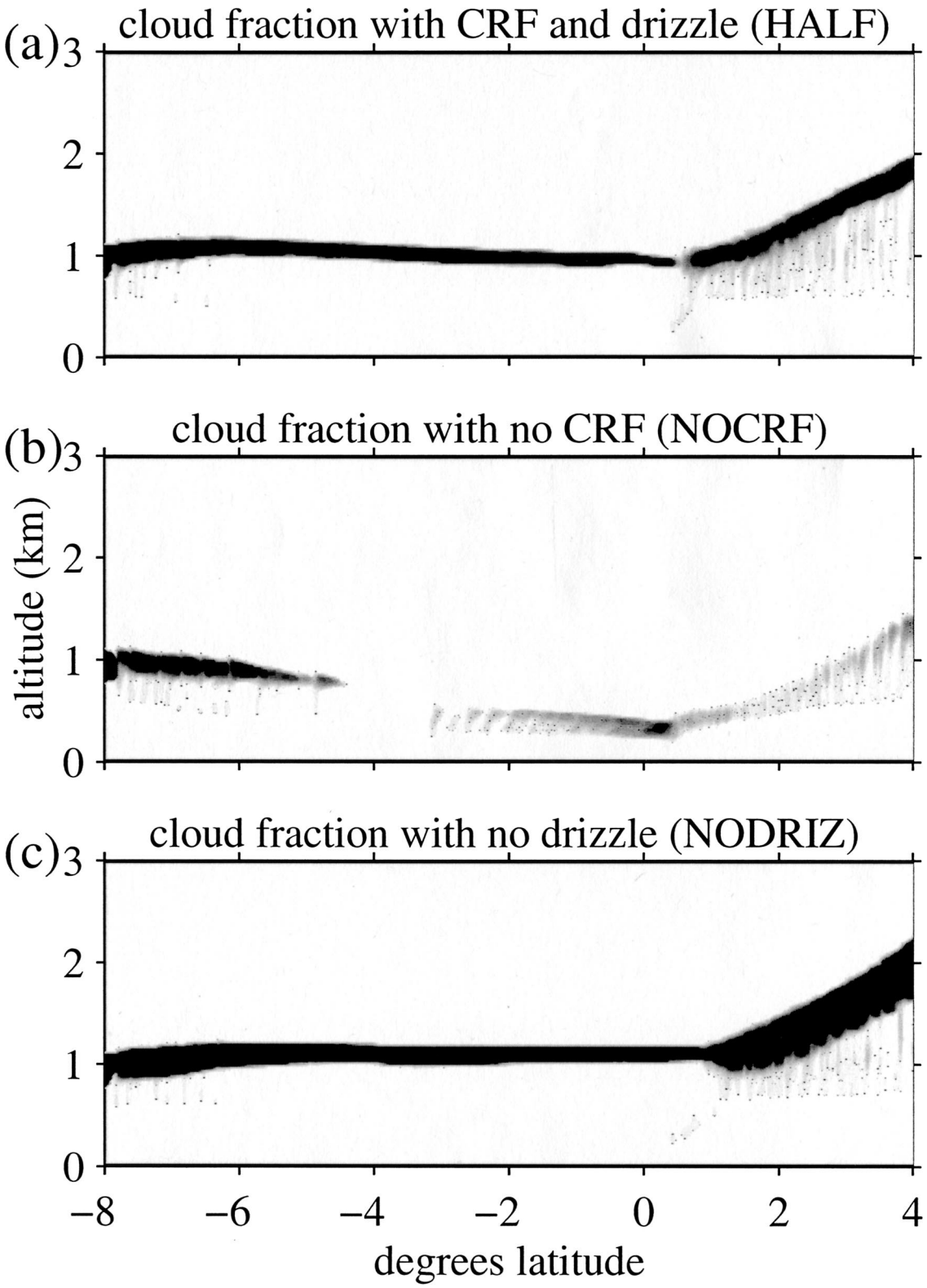

FIG. 16. Horizontally averaged cloud fraction for simulation (a) HALF with cloud radiative forcing and drizzle, (b) NOCRF without cloud radiative forcing, and (c) NODRIZ without drizzle.

surface fluxes north of the warm SST front is even more sensitive to precipitation. It thickens to as much as 580 m in NODRIZ, compared to 270 m in HALF. The ABL deepens more rapidly in NODRIZ due to increased turbulence and entrainment driven by the thicker clouds. We conclude that precipitation does not qualitatively change the simulated ABL evolution, but has surprisingly large quantitative effects.

3) LARGE-SCALE ZONAL ADVECTION

The justification for our meridionally quasi-Lagrangian approach is that, since zonal SST gradients are much weaker than meridional SST gradients in this region, zonal advection is comparatively unimportant to the ABL evolution. This is tested in simulation NOZONADV, in which the zonal advection sources are removed from HALF. In NOZONADV, the air–sea surface temperature difference between 5°S and the equator becomes 0.1°–0.2°C more positive (stable) than in BASE (not shown), drawing the simulation slightly further from observations. Zonal advective cooling then has small but significant cooling (destabilizing) effect on the surface air temperature. It has little impact on the cloud distribution, because the zonal gradients are small. The meridional advection included implicitly in the quasi-Lagrangian method is still critical to the simulation of the clouds.

c. Cloud hysteresis

In section 3c, we proposed a form of ''cloud hysteresis''—in which a cloud sustains itself across the cold tongue by its own radiative cooling—that may be important over the cold tongue, where no other appreciable cooling or moistening sources exist. Our Lagrangian model simulates the meridional evolution of a cloud layer in a single column of air. An Eulerian viewer would interpret cloud hysteresis as an advective effect. Over the cold tongue, clouds would prevail when clouds had advected from upstream. The degree to which advection affects the cloudiness in observations deserves more study. From the LES perspective, we might expect that cloudiness over the cold tongue should depend strongly on the cloudiness of the column when it enters the cold tongue region. We tested this dependence by performing simulations identical to HALF, except for different initial conditions. Since the cloud fraction is almost 100% across the cold tongue in our baseline simulation, in these simulations we reduced the initial ABL specific humidity to inhibit cloud formation.

Figure 17 shows the three initial humidity profiles that we will compare: HALF, a simulation IQM1 with a 1 g kg^{-1} drier ABL, and a simulation IQM2 with a 2 g kg^{-1} drier ABL. At the initial time, the ABL extends to 1.2 km.

The results in Fig. 18 vividly illustrate the nonlinear effect of changing the initial moisture profile. IQM1

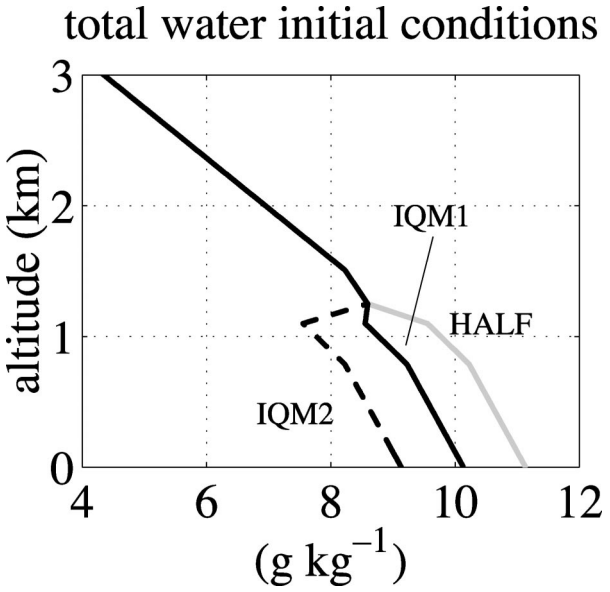

FIG. 17. Initial mixing ratio for the HALF (gray), IQMI (black), and IQM2 (dashed).

develops a stratocumulus cloud layer within 6 h then behaves much like HALF. IQM2 has an entirely different character. Though intermittent wisps of cloud form in the vicinity of 6°S, no persistent stratocumulus clouds ever form, and over the cold tongue the simulation resembles NOCRF. The ABL is too dry to form significant cloud before surface latent heat fluxes start to plummet as the column advects over the cold tongue. Without clouds, radiative cooling is inadequate to promote cloud formation until the ABL becomes much shallower, as happens near 2°S. Here, because the boundary layer is less than 700 m deep, the cold sea surface is able to moisten and cool this shallow layer enough to get condensation at its top. Very shallow stable boundary layers with fog were sometimes observed over the cold tongue during EPIC 2001 (Raymond et al. 2004), but we have not studied their relationship to upstream ABL cloudiness.

d. Humidity above the ABL

During EPIC 2001, the humidity of the free troposphere above the ABL was quite variable (Raymond et al. 2004). The free-tropospheric relative humidity chosen for the baseline simulation represents a typical humidity observed above the ABL. We ran a case DRY with the relative humidity reduced 40% everywhere above the inversion by changing the water vapor profile to which the free troposphere in the model was relaxed. Though the relaxation begins 150 m above the inversion, the drier free-tropospheric air still affects the jump across the inversion by subsiding onto the inversion.

In DRY, the net radiative cooling of the ABL increases about 10 W m^{-2} compared to HALF, due to

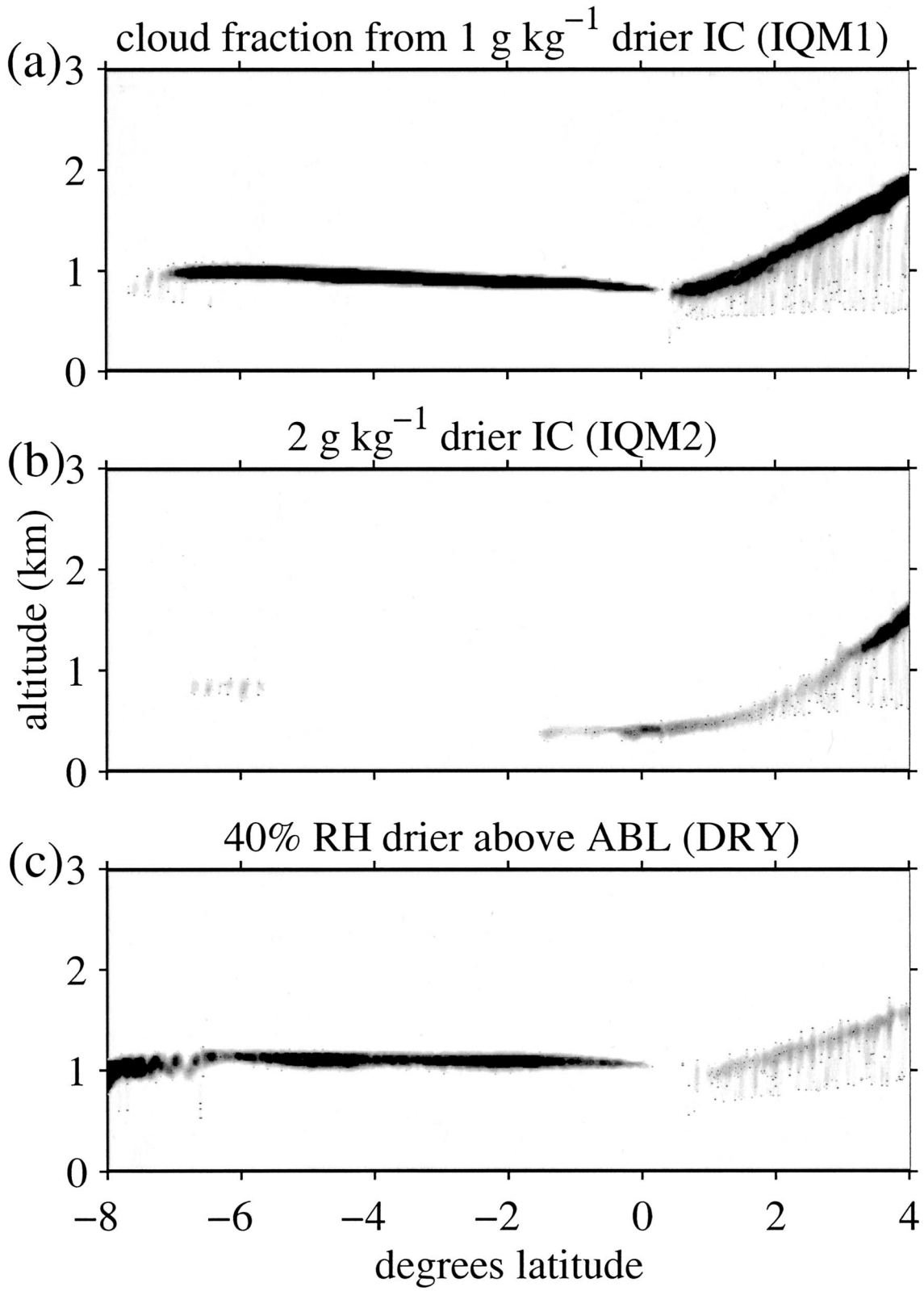

FIG. 18. The horizontally averaged cloud fraction from (a) the 1 g kg^{-1} (IQM1) and (b) the 2 g kg^{-1} (IQM2) drier initial conditions, and (c) 40% reduced relative humidity above the ABL (DRY).

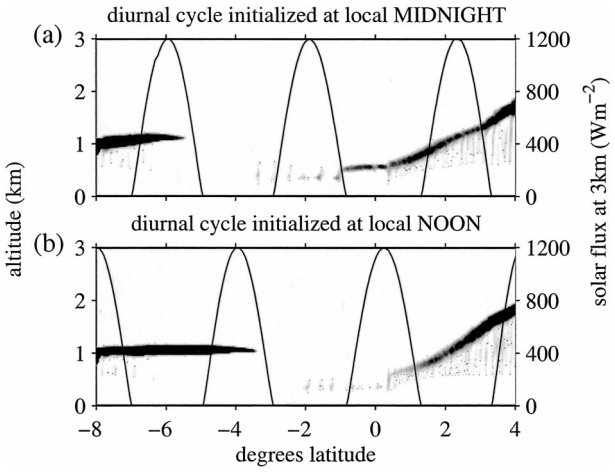

FIG. 19. The cloud fraction for (a) MIDNIGHT and (b) NOON, which have diurnally varying insolation. At 8°S, MIDNIGHT is initialized at local midnight, and NOON is initialized at local noon.

decreased downwelling longwave radiation associated with a less emissive lower troposphere. This slight increase in radiative cooling causes a marginal increase in entrainment over the cold tongue, which is responsible for about 5 W m^{-2} of entrainment-driven ABL warming. This partly compensates the radiative cooling, resulting in a small (5 W m^{-2}) net cooling of the ABL over the cold tongue. Although there is also enhanced entrainment drying in DRY, the cooling keeps the cloud from thinning substantially over the cold tongue.

Surprisingly, the cloud fraction is more substantially reduced in DRY—to less than 70%—in the surface-flux-driven regions north and south of the cold tongue. In these regions of DRY, entrainment drying is large, and dominates the depression of the saturation specific humidity by the radiative cooling. The reduced cloud also noticeably diminishes the ABL entrainment deepening north of 1°N.

e. The diurnal cycle

The simulations shown above all were forced by diurnally averaged insolation. The diurnal cycle interferes with the persistence of thin stratocumulus clouds, which can be evaporated by strong midday solar absorption. Simulations MIDNIGHT and NOON (Fig. 19) include the diurnal cycle of insolation. MIDNIGHT is initialized at 8°S at local midnight, and NOON at local noon. As a guide to the diurnal phase, the insolation at the top of the domain is overplotted. In both cases, once the stratocumulus cloud advects over the cold tongue region between 6°S and the equator, it evaporates at 1500 local standard time (LST) and does not reform in the evening. After the cloud evaporates, the ABL depth collapses, and only thin, low, intermittent clouds form until the column reaches the SST front. The large rectified effect of the diurnal cycle compared to BASE accentuates the role of simulated cloud radiative feedbacks over the cold tongue region. Once clouds have been evaporated by afternoon heating, they cannot form again over the cold region, because they cannot exist in the absence of both surface moisture flux and cloud-top radiative cooling. This rectified effect on cloud thickness and ABL depth gradually diminishes north of the SST front, and by 4°N has largely disappeared. At the end of the simulation, the cloud top is only about 50 m lower in MIDNIGHT and NOON than in BASE.

In reality, rather than the single 3.2 km × 3.2 km stratocumulus cloud we are able to simulate, the cross-equatorial ABL contains an ensemble of stratocumulus clouds and clear patches that vary on the mesoscale. This ensemble will be modulated by the diurnal cycle, but it is less likely that all the clouds in the ensemble would evaporate than it is that our simulated thin stratocumulus cloud would evaporate. On average, mesoscale variability might mitigate the effect of the diurnal cycle, consistent with frequent observations of stratocumulus over the cold tongue even during the afternoon (Rozandaal et al. 1995).

5. Conclusions

Our quasi-Lagrangian LES simulations elucidate some of the physical processes contributing to the distinctive south-to-north evolution of the ABL associated with cross-equatorial flow in the eastern equatorial Pacific. The LES permits surface, turbulence, and radiative processes, while prescribing the gross influence of pressure gradients and zonal advection. Different processes are important over the cold tongue (0°–5°S) than over the warm water to its north (0°–5°N). Over cold water, surface fluxes are negligible, and radiative flux divergence at the top is the only source of turbulence. Except for the cloud layer, the ABL is nearly laminar on the scales (>100 m) resolved by the LES, and modeled turbulent flux is mostly subgrid-scale. Over the warm water, surface sensible heat flux drives vigorous convective mixing—well resolved by the LES—and latent heat flux moistens the boundary layer. The subtle interaction of the thermodynamics and the pressure gradients expected around the SST front is not simulated by this method.

Over the cold water, we find that simulated stratocumulus cloud persists by radiative cooling at its top, but if the stratocumulus evaporates, it does not form again. Due to the moistness of the above-ABL air in the east Pacific, entrainment warms but does not dry the ABL. In the initially clear ABL, there is no turbulent entrainment and the ABL top is pushed down by subsidence. In the cloudy ABL, cloud-top radiative cooling drives turbulence and entrainment. The overlying air is moist, so the effect of entrainment is to keep the ABL top above the lifting condensation level allowing clouds to persist. Mesoscale variability and the diurnal cycle tend to reduce the distinct persistence of the modeled

cloud. However, the efficacy of cloud-top radiative cooling in maintaining clouds means that the cloudiness over the cold tongue is likely determined somewhat by advection of cloudiness from the southeast. Observations should be analyzed to see to what degree variability in the cold-tongue cloudiness can be explained by cloudiness advection. The interplay of clouds, radiation, entrainment, and advection is an ongoing area of research in ABL parameterizations for large-scale models.

The LES corroborates WMD's argument that the low surface wind over the cold tongue can be explained by the vertical distribution of momentum. Low surface winds are accompanied by a 500-m wind jet, which ''slips'' across the cold tongue. Large-scale advection cools the ABL south of the equator and slightly reduces the stability of the air–sea interface. Due to the surface stability, surface drag is confined in a very shallow layer below the jet, slowing the surface winds. Unimpeded by friction, the elevated jet accelerates due to the meridional pressure gradient, which is strongest at the surface.

North of the warm SST front, where the air–sea interface is unstable, the LES-simulated dynamics are also consistent with WMD. The latent heat flux drives the formation of stratocumulus, which deepen into cumulus rising into stratocumulus. The ABL gradually deepens due to vigorous turbulent entrainment amplified by the cloud feedbacks. Drizzle dries the stratocumulus clouds over the warm SST, keeping the modeled clouds from becoming unrealistically thick. The convection also remixes the previously decoupled internal stable and sheared layers of the ABL. The jet is recoupled to the surface, causing a transient surge in the surface wind. Once the momentum jet has been mixed through the ABL and dissipated by surface friction, the surge in the surface wind declines.

The steady response of the surface wind to the warm SST is to continually balance the pressure gradient force with the surface friction. The steady increase in surface wind speed causes a region of wind stress divergence over the warm SST front. The modeled transient wind increase sharpens the divergence close to the front, and causes weak convergence north of the wind maximum. How this wind stress pattern on the ocean feeds back on the SST front, the tropical instability waves, and the large-scale ocean currents remains an interesting question.

The vertical resolution of our model was too coarse to resolve turbulent processes over the cold tongue, for example, the interaction of the jet and the surface layer. A shorter simulation with finer vertical resolution would capture these effects, as well as the sudden ABL evolution as air advects across the SST front.

Our quasi-Lagrangian framework is attractive for comparison with single-column models, which test the physical parameterizations used in regional models and GCMs. The EPIC 2001 dataset provides a rich validation for single-column models due to the variety of ABL processes that are relevant in the east Pacific region. We hope that our forcings are applied to test single column models, and we plan to test one such model, the National Center for Atmospheric Research (NCAR) single-column community atmosphere model. In addition, our LES simulations may be a useful comparison with 95°W cross sections from full three-dimensional GCMs and regional simulations.

Acknowledgments. We thank Dr. David Stevens of LLNL for providing the original LES code. We would also like to acknowledge support from NSF Grants ATM-0082384 and ATM-0082391.

REFERENCES

Bond, N. A., 1992: Observations of planetary boundary layer structure in the eastern equatorial Pacific. *J. Climate,* **5,** 699–706.

Bretherton, C. S., S. K. Krueger, M. C. Wyant, P. Bechtold, E. van Meijgaard, B. Stevens, and J. Teixeira, 1999a: A GCSS boundary-layer cloud model intercomparison study of the first ASTEX Lagrangian experiment. *Bound.-Layer Meteor.,* **93,** 341–380.

——, and Coauthors, 1999b: An intercomparison of radiatively driven entrainment and turbulence in a smoke cloud, as simulated by different numerical models. *Quart. J. Roy. Meteor. Soc.,* **125,** 391–423.

——, T. Uttal, C. W. Fairall, S. Yuter, R. Weller, D. Baumgardner, K. Comstock, and R. Wood, 2004: The EPIC 2001 stratocumulus study. *Bull. Amer. Meteor. Soc.,* in press.

Chelton, D. B., and Coauthors, 2001: Observations of coupling between surface wind stress and sea surface temperature in the eastern tropical Pacific. *J. Climate,* **14,** 1479–1498.

Deser, C., 1993: Diagnosis of the surface momentum balance over the tropical Pacific Ocean. *J. Climate,* **6,** 64–74.

Fairall, C. W., E. F. Bradley, D. P. Rogers, J. B. Edson, and G. S. Young, 1996: Bulk parameterization of air–sea fluxes for Tropical Ocean-Global Atmosphere Coupled-Ocean Atmosphere Response Experiment. *J. Geophys. Res.,* **101,** 3747–3764.

Gabriel, P. L., P. T. Partain, and G. L. Stephens, 2001: Parameterization of atmospheric radiative transfer. Part II: Selection rules. *J. Atmos. Sci.,* **58,** 3411–3423.

Hashizume, H., S. Xie, M. Fujiwara, T. Shiotani, M. Watanabe, Y. Tanimoto, W. T. Liu, and K. Takeuchi, 2002: Direct observations of atmospheric boundary layer response to SST variations associated with tropical instability waves over the eastern equatorial Pacific. *J. Climate,* **15,** 3379–3393.

Hayes, S. P., M. J. McPhaden, and J. M. Wallace, 1989: The influence of sea-surface temperature on surface wind in the eastern equatorial Pacific: Weekly to monthly variability. *J. Climate,* **2,** 1500–1506.

Lindzen, R. S., and S. Nigam, 1987: On the sole of sea surface temperature gradients in forcing low-level winds and convergence in the Tropics. *J. Atmos. Sci.,* **44,** 2418–2436.

McGauley, M., C. Zhang, and N. Bond, 2004: Large-scale characteristics of the atmospheric boundary layer in the eastern Pacific cold tongue–ITCZ region. *J. Climate,* in press.

Ogura, Y., and N. Phillips, 1962: Scale analysis of deep and shallow convection in the atmosphere. *J. Atmos. Sci.,* **19,** 173–179.

Raymond, D. J., S. K. Esbensen, M. Gregg, and C. S. Bretherton, 2004: EPIC 2001 and the coupled ocean–atmosphere system of the tropical east Pacific. *Bull. Amer. Meteor. Soc.,* in press.

Rozendaal, M. A., C. B. Leovy, and S. A. Klein, 1995: An observational study of diurnal variations of marine stratiform cloud. *J. Climate,* **8,** 1795–1809.

Smagorinsky, J., 1963: General circulation experiments with the primitive equations. *Mon. Wea. Rev.*, **91,** 99–164.

Stephens, G. L., P. L. Gabriel, and P. T. Partain, 2001: Parameterization of atmospheric radiative transfer. Part I: Validity of simple models. *J. Atmos. Sci.*, **58,** 3391–3409.

Stevens, B., J. Duan, J. C. McWilliams, M. Munnich, and J. D. Neelin, 2002: Entrainment, Rayleigh friction and boundary layer winds over the tropical Pacific. *J. Climate,* **15,** 30–44.

Stevens, D. E., and C. S. Bretherton, 1996: A forward-in-time advection scheme and adaptive multilevel flow solver for nearly incompressible atmospheric flow. *J. Comput. Phys.*, **129,** 284–295.

Thum, N., S. K. Esbensen, D. B. Chelton, and M. J. McPhaden, 2002: Air–sea heat exchange along the northern sea surface temperature front in the eastern tropical Pacific. *J. Climate,* **15,** 3361–3378.

Tomas, R. A., J. R. Holton, and P. J. Webster, 1999: The influence of cross-equatorial pressure gradients on the location of near-equatorial convection. *Quart. J. Roy. Meteor. Soc.*, **125,** 1107–1127.

Wakefield, J. S., and W. H. Schubert, 1981: Mixed-layer model simulation of eastern North Pacific stratocumulus. *Mon. Wea. Rev.*, **109,** 1952–1968.

Wallace, J. M., T. P. Mitchell, and C. Deser, 1989: The influence of sea-surface temperature on surface wind in the eastern equatorial Pacific: Seasonal and interannual variability. *J. Climate,* **2,** 1492–1499.

Wood, R., and C. S. Bretherton, 2004: Boundary layer depth, entrainment, and decoupling in the cloud-capped subtropical and tropical marine boundary layer. *J. Climate,* in press.

Wyant, M. C., C. S. Bretherton, H. A. Rand, and D. E. Stevens, 1997: Numerical simulations and a conceptual model for the stratocumulus to trade cumulus transition. *J. Atmos. Sci.*, **54,** 168–192.

Yin, B. F., and B. A. Albrect, 2000: Spatial variability of atmospheric boundary layer structure over the eastern equatorial Pacific. *J. Climate,* **13,** 1574–1592.

Zeng, X., M. A. Brunke, M. Zhou, C. Fairall, N. A. Bond, and D. H. Lenschow, 2004: Marine atmospheric boundary layer height over the eastern Pacific: Data analysis and model evaluation. *J. Climate,* in press.